Effects of Experimental Conditions on Fracture Research Using 3D Printed Materials

by

Majed Abdulsattar Almubarak

B.S. Petroleum Engineering
Texas A&M University (2019)

Submitted to the Department of Civil and Environmental Engineering
in partial fulfillment of the requirements for the degree of

Master of Science in Civil and Environmental Engineering

at the

MASSACHUSETTS INSTITUTE OF TECHNOLOGY

June 2023

Authored by: Majed Almubarak
Department of Civil and Environmental Engineering
May 12, 2023

Certified by: Herbert H. Einstein
Professor of Civil and Environmental Engineering
Thesis Supervisor

Accepted by: Colette L. Heald
Professor of Civil and Environmental Engineering
Chair, Graduate Program Committee

Effects of Experimental Conditions on Fracture Research Using 3D Printed Materials

by

Majed Abdulsattar Almubarak

Submitted to the Department of Civil and Environmental Engineering
on May 12, 2023, in partial fulfillment of the
requirements for the degree of
Master of Science in Civil and Environmental Engineering

Abstract

The fracturing behavior and mechanical characterization of rocks are important for many applications in the fields of civil, mining, geothermal, and petroleum engineering. Laboratory testing of rocks plays a major role in understanding the underlying processes that occur on the larger scale and for predicting rock behavior. Fracturing research requires well-defined and consistent boundary conditions. Consequently, the testing design and setup can greatly influence the results.

In this study, a comprehensive experimental program using an artificial material was carried out to systematically evaluate the effects of different parameters in rock testing under uniaxial compression. The parameters include post-processing curing, printing orientation, compression platen type, specimen centering, loading control method and rate, specimen size, specimen cross-sectional geometry, boundary constraints, and flaw parameters.

The specimens were prepared using a 3D stereolithography printer utilizing clear resin material. Identical pre-existing quasi-elliptical (ovaloid-shaped) flaws were placed in the center of each specimen. The specimens were subjected to unconfined compression using a Baldwin load frame. The testing setup included a high-speed camera and a high-resolution camera for visual analysis of the fracturing processes.

The results show that these testing conditions have a significant effect on the mechanical behavior of rocks. Post-processing curing increases the strength of the material, with longer curing times resulting in higher material strength. Different printing orientations exhibit varying strengths. Using a fixed compression platen helped reduce bulging of the material. Centering of the specimen played a critical role to avoid buckling and unequal distribution of stress. Slower displacement rates can control the energy being released once failure occurs to prevent the specimen from exploding. Larger specimens generally fail at lower stresses compared to smaller specimens. Also, the frictional end effects were investigated by comparing lubricated and non-lubricated end conditions. Very importantly, the study also identified variations in crack initiation and propagation between specimens with internal flaws and specimens with throughgoing flaws. This investigation showed that tensile wing cracks

appeared in specimens with throughgoing flaws, while wing cracks with petal cracks were associated with the internal flaws. It also showed that the mechanical properties are influenced by the inclination of the flaws and established that specimens with internal flaws generally exhibit higher material strength compared to specimens with throughgoing flaws.

The systematic analysis presented in this work sheds light on important considerations that need to be taken into account when conducting fracture research and adds knowledge to the fundamental understanding of how fractures occur in nature.

Thesis Supervisor: Herbert H. Einstein
Title: Professor of Civil and Environmental Engineering

Acknowledgments

To say that my journey since starting at MIT has been challenging would be an understatement. Nevertheless, I am proud to be where I am today. I have learned so much from this experience, most importantly I have developed as a person and as a researcher. I owe this to my support system and to everyone who helped me reach this point.

I am most thankful to my advisor, Professor Herbert H. Einstein for his invaluable care and guidance. His passion motivates me to work hard toward my goals. He has been beyond supportive and selfless, helping me tackle so many challenges. I am very honored to be one of his students and a member of his research group. I am also thankful to Professor John Germaine (Dr. G) for his support, expertise, and advice on conducting experiments and use of laboratory equipment. I am also indebted to Stephen Rudolph for providing valuable help in laboratory needs and setting up the experiments.

I have sincere appreciation for my research group: Hao Kang, Omar AlDajani, Rafael Villamor Lora, Paris Smalls, Ignacio Arzuaga Garcia, Randy Pietersen, Eve Meltzer, and Beatriz Goncalves Klink for making me feel welcome and providing constructive feedback during our Monday meetings. Also, thanks to Magreth Kakoko for acquainting me with 3D printing and walking me through my first CAD designs.

I am also grateful to my friends: Mahmoud Ramadan, Maad Alzayer, Tony Tohme, Julio Hernandez, Omar Al-Saeedi, Nathan Tshizubu, Khaled Aldhayee, and Jun Hong Ng for all their support.

Most importantly, I would like to thank my parents, my brother Tariq, and my sisters Sama and Yara, who have supported me at every step of my journey from day one. Without their encouragement, I would not have become the person I am today.

I also hold huge gratitude to my late professor at Texas A&M University, Dr. Hisham Nasr-El-Din, for guiding me throughout my undergraduate research and encouraging me to pursue graduate education. May Allah bless his soul and award him the highest level of heaven.

Contents

List of Figures

List of Tables

Chapter 1

Introduction

1.1 Motivation

Fractures are the most common structural features that are found in all types of rocks and tectonic settings. Consequently, extensive research, including laboratory testing, has been conducted in this area. Laboratory testing has played an important role in characterizing the strength of rocks and understanding fracture behavior (Xu et al., 2016). Numerous efforts have been made to investigate the mechanical and fracture properties of rocks and rock-like materials under compressive loading. Many of these studies were done on prismatic specimens of gypsum, marble, granite, and shale (Reyes, 1991; Bobet, 1997; Wong, 2008; Miller, 2008; Gonçalves da Silva, 2009; and Morgan, 2015). In these studies, specimens were subjected to uniaxial compressive loading, and then fracture initiation and propagation mechanisms were captured and analyzed.

Despite a considerable amount of experimental and theoretical studies conducted in this field, there is still a lack of knowledge on the exact mechanisms of many fracture related processes. In this context, two areas of interest were identified to look at in more detail. The first involved identifying and varying critical boundary conditions associated with rock testing. The second pertains to the design of the pre-existing defects, commonly referred to as "flaws," and the subsequent investigation of how these flaws influence the fracturing processes during rock testing.

1.2 Research Objectives

As stated above the main objectives of this research are two-fold. The first is to discuss the apparatus, instrumentation, specimen properties, and procedures used to systematically conduct rock fracturing experiments. The parameters investigated include: process parameters (post-processing curing and printing orientation), the type of compression platen used (fixed vs. flexible), specimen centering, loading control method (displacement vs. load) and rate, specimen size, cross-sectional geometry, and frictional end effects (fixed vs. lubricated boundaries). The second objective is to conduct a systematic study comparing the fracture processes in rock experiments with internal flaws to those with throughgoing flaws.

In the majority of previous investigations, flaws were fully penetrating or throughgoing, while natural rock formations often possess internal flaws rather than throughgoing ones. To date, there has not been a comprehensive study employing fully comparable geometries exploring the similarity or difference between fracture processes in rock experiments with throughgoing flaws and those with exclusively internal flaws.

There are two primary challenges in experimentally investigating internal flaw specimens. The first challenge is difficulties in producing specimens with controlled internal flaw geometries. The second challenge lies in the difficulty of monitoring the propagation of internal fractures. Hence, the investigations reported in this work are conducted with an artificial material.

In general, it is important to understand how these factors affect rock fracturing experiments so that we can choose them carefully and get the most consistent results.

1.3 Thesis Structure

The remainder of the thesis is organized as follows:

- Chapter 2: Experimental Methods. This chapter details the experimental procedure, including the 3D printing process, material selection for printing specimens, specimen preparation, test setup with the Baldwin load frame, and monitoring components like high-resolution and high-speed cameras. Additionally, it discusses the test program, which covers load, axial displacement, and time data synchronization with image frames captured during the experiments.

- Chapter 3: Results and Discussion. This chapter discusses the investigated parameters in detail, presents results as true stress versus strain plots for uniaxial experiments, compares yield stress and ultimate compressive stress values, and examines visual observations of specimens during testing.

- Chapter 4: Conclusions and Recommendations. This chapter presents a summary of the work done and conclusions drawn from the results. Future research recommendations are also discussed.

Chapter 2

Experimental Methods

2.1 Introduction

A comprehensive study was carried out on the influence of various process parameters, equipment and testing conditions, specimen parameters, flaw parameters, and boundary constraints on rock testing through a series of uniaxial compression tests. The purpose and specific details of each of these tests appear later in Chapter 3.

A range of 3D printed prismatic specimens of varying sizes, cross-sectional shapes, and flaw specifications were tested. This chapter provides an in-depth description of the experimental procedure, starting with an overview of 3D printing technology followed by a description of the material used to print the specimens. The specimen preparation process is then outlined, including the important steps that must be taken to ensure that the specimens are ready for testing. The test setup including the Baldwin load frame used for the compression tests is described in detail, as well as the various components that were used to track the fracturing processes, such as the high-resolution and high-speed cameras. Finally, the test program is discussed, including the important details such as the load, axial displacement, and time data that were recorded for all experiments and synchronized with the image frames captured by the cameras.

2.2 3D Printing Technology

Creative individuals possess the potential to envision innovations that could transform various industries. However, these conceptual ideas hold only theoretical value within the minds of their originators. The tangible worth of such inventions can only be fully appreciated upon the production of a functional prototype. While the transition from ideation to materialization may appear straightforward, the process typically demands a considerable amount of time. Numerous inventors face challenges during the prototyping phase, as the development of a successful prototype is often preceded by numerous iterations of unsuccessful prototypes.

Hideo Kodama, from the Nagoya Municipal Industrial Research Institute of Japan, is credited with initiating a significant revolution in prototype manufacturing in 1981. Recognizing the temporal challenges associated with invention and prototyping, Kodama sought to transform the production of individual prototype components to be faster, more cost-effective, and less labor-intensive. Kodama (1981) proposed that, rather than removing material to achieve a design, computers and specialized equipment could employ a novel method of fabricating solid objects through "additive manufacturing," thereby accelerating prototyping and manufacturing processes.

Kodama designed and constructed a functional machine to realize his vision of rapid prototyping (RP) additive manufacturing, for which he filed a patent application in 1981. This particular device utilized an XY two-dimensional plotter connected to an ultraviolet (UV) light source via an optical fiber. Beneath the plotter was a movable plate situated in a receptacle filled with a liquid mixture of unsaturated polyester, a polymer cross-linking agent, and a polymerization initiator. The plotter was programmed to trace a specific path, emitting UV light to form individual layers of the designated design. The UV light was directed to specific areas of the resin reservoir by a mask, initiating the polymerization process in the reservoir of photo-hardening polymer resin, and allowing the individual layers to solidify directly onto the preceding layers. The schematics of Hideo Kodama's product are shown in Figure 2-1.

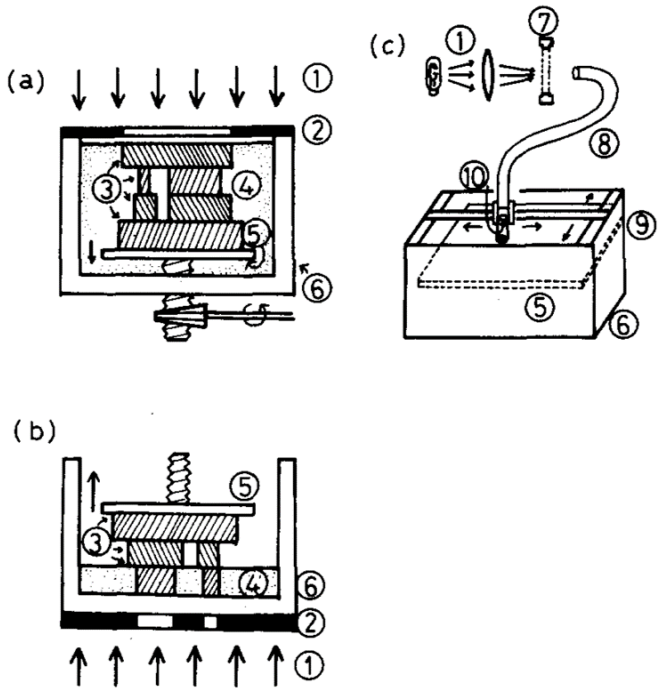

FIG. 1. Schematic sketches of three types of apparatus constructed in the present work. In this Fig. ① ultraviolet rays ② mask ③ solidified layers ④ liquid photo-hardening polymer ⑤ movable plate ⑥ receptacle ⑦ shutter ⑧ optical fiber ⑨ *XY* plotter and ⑩ optical lens. Exposure and shift of the movable plate is repeated in turn, and the solid model is grown on or under the plate.

Figure 2-1: Hideo Kodama's schematic sketches and the original caption detailing his design components (Kodama, 1981).

There has been an interest in using artificial model materials for as long as mechanical testing of rocks has been performed. Rapid prototyping (RP), additive manufacturing (AM), and three-dimensional printing (3DP) are three interchangeable terms that define a set of methods for the fast, precise, and repeatable production of elements (Zhou and Zhu, 2018). The technology is based on the process of joining materials layer by layer to form an object using computer-aided design (CAD). Polymeric, metallic, ceramic, and even complex composite components are among the materials used (Ngo et al., 2018). Various 3DP techniques have been developed, including fused deposition manufacturing (FDM), stereolithography (SLA), and selective laser sintering (SLS).

2.2.1 SLA 3D Printing

Compared to other 3DP techniques, SLA is one of the earliest and most widely used (Vaezi et al., 2013). SLA is also one of the most popular AM techniques for polymeric and ceramic materials, as it produces components with high geometrical precision and superior mechanical properties (Melchels et al., 2010). Printing with a special photocurable resin is the basis of the SLA method (Gao et al., 2021). The liquid photopolymer resin is cured layer-by-layer using an ultraviolet (UV) laser. After a layer is cured, the build plate adjusts, and the next successive resin layer is cured. The process of the resin being crosslinked under UV light exposure is called photopolymerization (Hamzah et al., 2018).

When exposed to UV light, photo-initiators in the photopolymer produce free radicals (Watters and Bernhardt, 2018). In an exothermic reaction, the free radicals react with monomers and oligomers within the resin to cross-link and create a network of polymer chains as shown in Figure 2-2. More specifically, the photo-initiator molecule breaks down into two parts in response to UV exposure, and the bond that holds it together becomes two highly reactive radicals. The reactive radicals are transferred by the photo-initiator to the active groups on the monomer and oligomer chains, which in turn react with other active groups to form longer chains (Riccio et al., 2022). The process is extremely quick, taking only milliseconds.

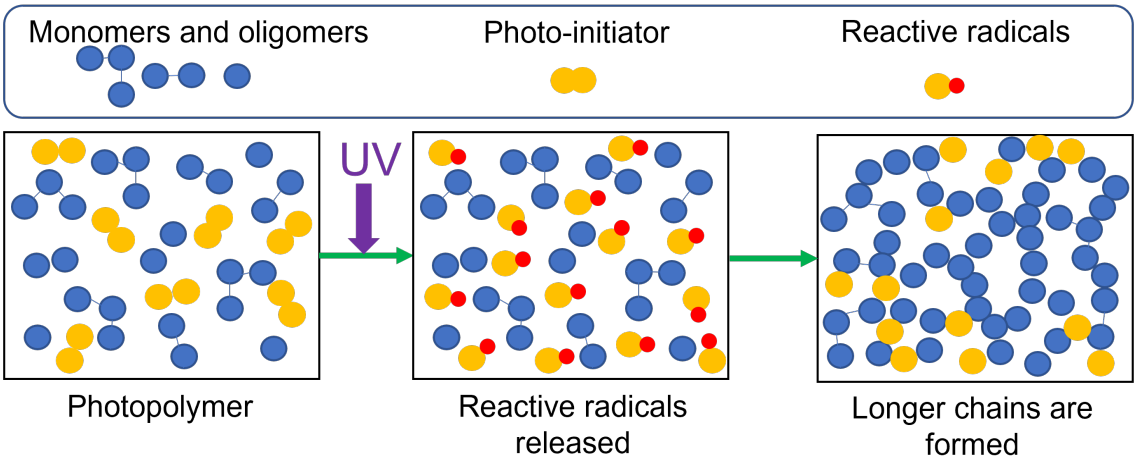

Figure 2-2: Photopolymerization scheme of SLA resin.

2.2.2 Basic Material Testing and Selection

The study utilized specimens produced from clear resin material using SLA 3D printing technology. The material properties were evaluated through uniaxial compression tests on two intact (no flaw) specimens with dimensions of 4 inches in height, 2 inches in length, and 2 inches in width as shown in Figure 3-1a. The specimens were equipped with both axial and lateral extensometers, as depicted in Figure 2-3b, to accurately measure their displacements during the testing process. The tests were run at a constant displacement rate of 1 millimeter per minute (mm/min), allowing for a controlled and systematic evaluation of the specimens' mechanical behavior under compression.

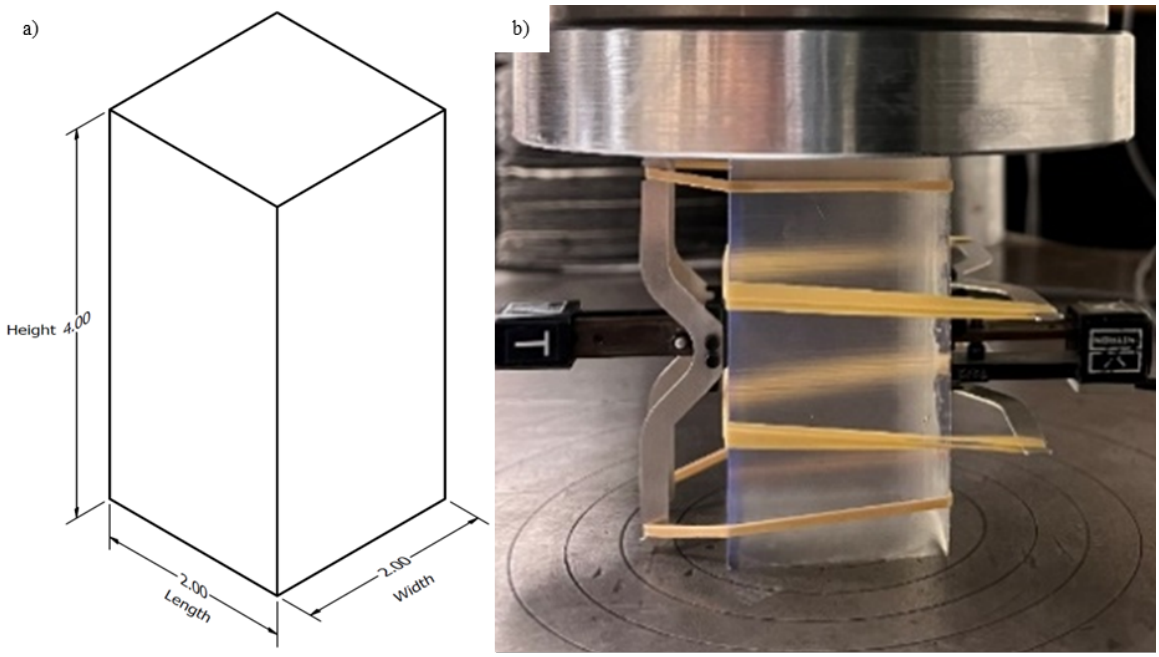

Figure 2-3: Details of prismatic intact specimen used to determine the material properties: a) rendering of the specimen with dimensions (4 in x 2 in x 2 in), b) photograph of specimen subjected to uniaxial loading with axial and lateral extensometers attached.

The elastic portion of the stress-strain curves of the tests is shown in Figure 2-4.

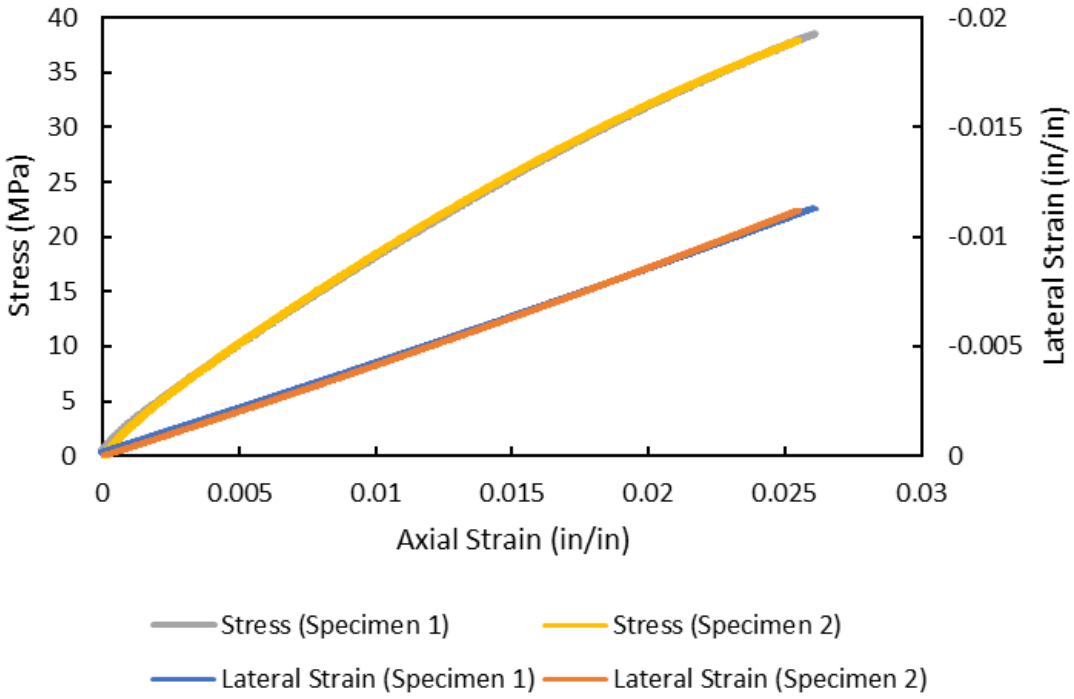

Figure 2-4: Stress-strain data acquired from uniaxial compression tests on two intact specimens (left vertical axis: stress, bottom axis: axial strain, right vertical axis: lateral strain).

The elastic constants of the material, Young's modulus (E) and Poisson's ratio (ν), are presented in Table 2.1.

Table 2.1: Elastic properties of intact 3D printed clear resin specimens subjected to uniaxial compression.

Specimen #	**E, MPa**	ν
1	1618.9	0.4312
2	1635.2	0.4301
Average	1627.1	0.4307

The use of 3D printing technology in this research provides several advantages. One of the most notable benefits is the ability to control the material properties and produce complex geometries that are otherwise difficult to obtain using traditional methods. This advantage is crucial when investigating the effects of different parameters on the material properties as it eliminates sample-to-sample variability (Kong et al., 2018). Moreover, this leads to more accurate and reproducible results. In this study, clear resin was chosen as the testing material due to its homogeneity and optically transparent nature. These properties make it an ideal choice for investigating the fracture processes and through photoelasticity the internal stress fields of the material (Wang et al., 2017). Also, the use of clear resin as the testing material provides insights into the behavior of the material during testing that would otherwise be impossible to observe with opaque materials.

2.3 Specimen Preparation

For this study, a series of specimens were prepared, each with a prismatic configuration and a height dimension that was twice the width. The most distinct feature of these specimens was the presence of a quasi-elliptical (ovaloid-shaped) flaw at the center of each specimen, as shown in Figure 2-5. The choice of a prismatic configuration and a height dimension twice the width was made to produce a uniform stress distribution across the specimen during the uniaxial compression tests. The addition of a flaw was also deliberate, making it possible to study the effect of flaws on the mechanical properties and fracture behavior of the material. These specimens with their unique geometries and flaw specifications were carefully chosen to make it possible for a comprehensive investigation of the different parameters and conditions involved in this study.

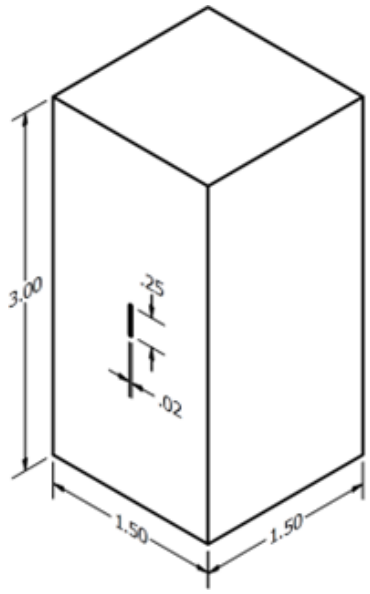

Figure 2-5: Example rendering of prismatic specimen used in this study including the pre-existing vertical flaw with rounded tips. The example shown has dimensions (3 in x 1.5 in x 1.5 in) and flaw dimensions (0.25 in x 0.02 in).

2.3.1 Specific 3D Printing Process

In this study, all specimens were fabricated using a commercial stereolithography (SLA) 3D printer equipped with a class 1 violet laser source. The laser specifications are: 250 mW power output, 85 micron spot size, and a nominal resolution of 25 microns. The clear photoreactive resin material used in the 3D printing process is composed of a mixture of methacrylated oligomer (comprising between 75% to 90% of the material), methacrylated monomer (between 25% to 50%), and a photo-initiator, diphenyl (2,4,6-trimethylbenzoyl) phosphine oxide (less than 1%). This high-quality resin material, as described by Marin et al. (2021), has proven to be suitable for creating precise and detailed specimens.

Creating physical objects using a 3D printer is a multi-step process that starts with designing a 3D CAD model using a suitable modeling software. After designing, the 3D model is saved as an STL file, which is a standard file format used in 3D printing. This STL file is then loaded into a slicing software that is compatible with the 3D printer being used. The slicing software is responsible for dividing the 3D model into many thin layers and creating a g-code that contains position sequences for the 3D printer to build the object layer by layer. The g-code is then sent to the 3D printer, which reads the code and starts the printing process. Once the printing process is complete, the 3D build platform is removed from the printer and the post-processing stage begins. The 3D printing scheme is summarized in Figure 2-6 below for easy visualization.

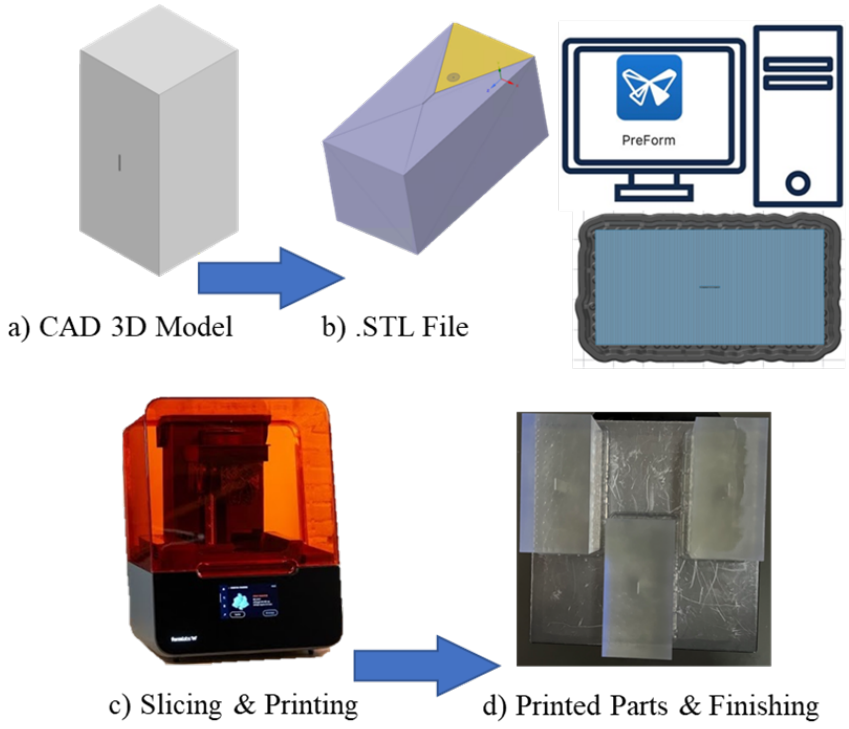

Figure 2-6: Summary of SLA 3D printing process: a) 3D CAD model generated using a modeling software, b) CAD model is converted to an STL file, c) printer software digitally slices the model in the STL file into a series of cross-sectional layers, assigns them with printing information (e.g., layer thickness and printing path), and instructs the SLA printer to print, d) 3D printing build platform is removed once printing is complete and the post-processing stage begins.

2.3.2 3D Printing-Related Software

The process of 3D printing involves the use of two different software modules. The first is the CAD software, which is used to create the specimens. The second software is used to convert the STL file generated by the CAD software and send it to the printer.

In this work, Autodesk Fusion 360 software was used to create the CAD model of the specimens. Autodesk Fusion 360 is a tool for computer-aided design (CAD) and product development. Its advanced modeling tools permit the creation of complex designs with precision.

Once a CAD model has been created using Fusion 360, the next step is to prepare it for 3D printing using Preform software. Preform is a specialized interface that enables users to make adjustments to their models in order to optimize them for 3D printing. By using Preform, one can adjust the orientation of the model and incorporate support structures. Additionally, it provides a visual representation of the final print, permitting users to identify potential issues before printing begins. This not only saves time but also reduces the risk of failed prints. A screenshot from the software is shown in Figure 2-7.

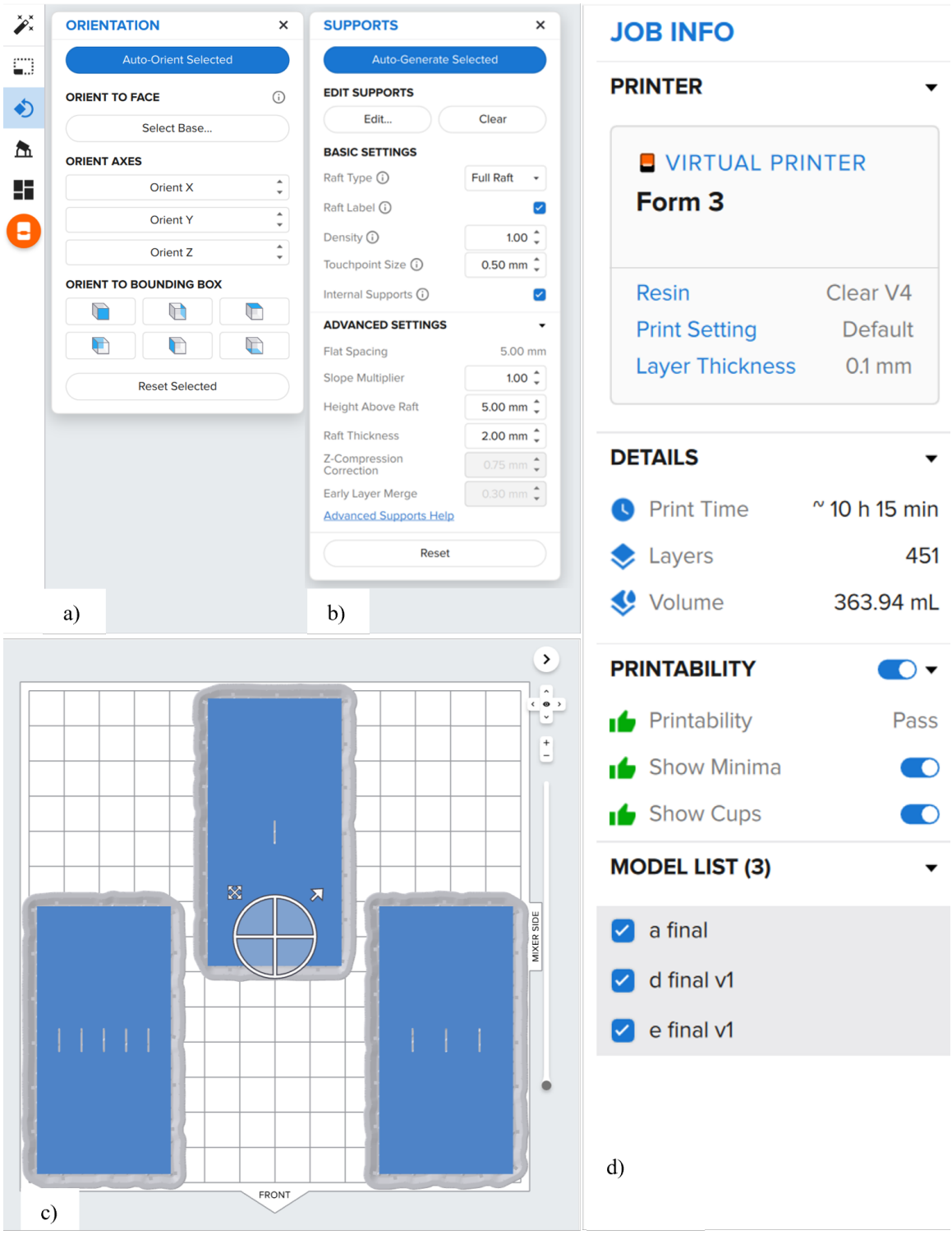

Figure 2-7: Screenshot image from Preform software showing: a) orientation settings, b) supports settings, c) a visualization of the specimens on the printing build platform, and d) print information details.

2.3.3 Specimen Post-Processing

The average printing duration was approximately 12 hours, for three specimens at a time. After the 3D printing process was completed, the build platform was inserted into an isopropyl alcohol (IPA) bath, which automatically rinses the specimens for 20 minutes. This step was crucial in ensuring the complete removal of any residual resin material, which could negatively affect the specimens. Following the rinse, the specimens were allowed to dry at room temperature for six hours. After this period, the specimens were released from the build platform, and the supports were removed. The setup of the 3D printer used in this study is shown in Figure 2-8.

Furthermore, the time between printing and testing was kept constant for all specimens to minimize any potential aging effects and accidental exposure to UV light, which might cause hardening and crosslinking of the polymers. This procedure was carried out in a similar manner for all the experiments to maintain consistency and provide a controlled environment for comparison.

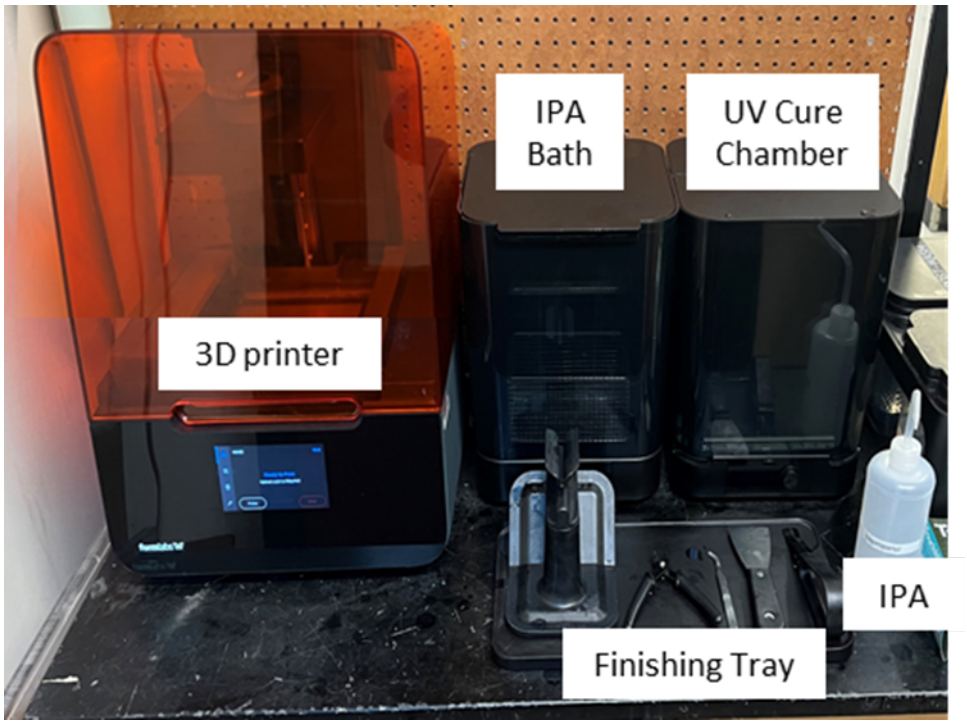

Figure 2-8: SLA 3D printer and post-processing setup.

2.3.4 Specimen Polishing

The final stage in the specimen preparation process involves polishing the front face of the specimens that face the camera, with the goal of achieving a high-quality video and photo recording during the test. This is accomplished by securing the specimen with a G-clamp and using sandpapers with decreasing grit sizes, starting with 220 (coarse) and progressing to finer sizes of 400, 800, and 1200, respectively. For each grit size, the specimen is polished for approximately 1 minute while alternating between horizontal and vertical polishing directions. Water is applied to both the specimen and sandpaper to avoid scratching and minimize friction during the process. The specimen is washed after each step to remove any residual polished material. Finally, three different polishing liquids, including a scratch remover and a shine enhancer, are applied to achieve a smooth, glossy surface. The images in Figure 2-9 demonstrate the contrast between the unpolished and polished surfaces.

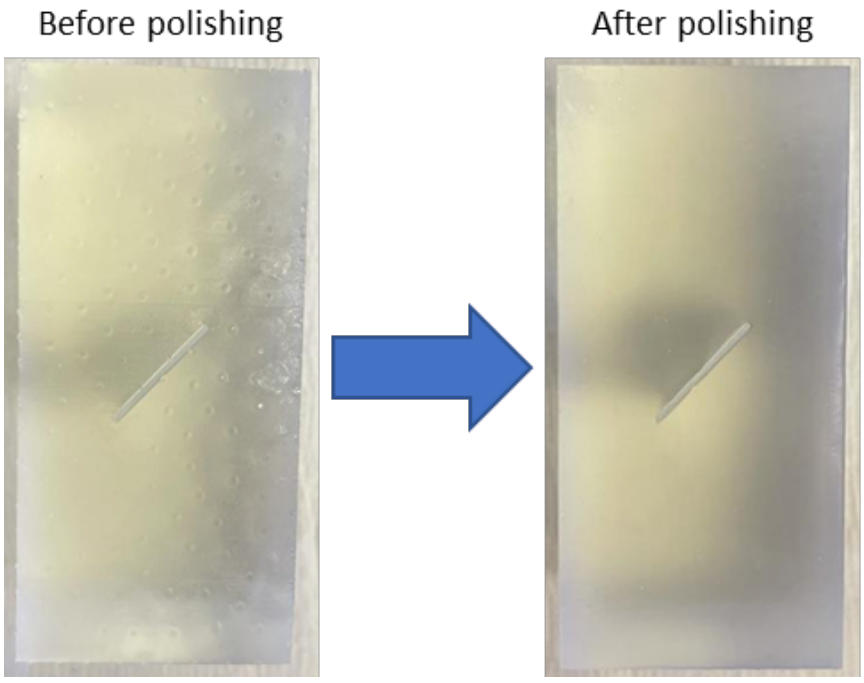

Figure 2-9: Images taken before and after polishing the specimen surface. The observed difference between the two is that the surface after polishing lacks the marks and bumps left by supports.

2.4 Test Setup

The specimens in this study were subjected to unconfined compression along the axial direction, also known as uniaxial compression. A Baldwin load frame, which is a hydraulic loading machine, was used for this purpose. The machine had a maximum loading capacity of 60 kips and an 8-inch stroke, allowing for sufficient force to be applied on the specimens during testing. The testing setup, as shown in the photograph in Figure 2-10, also included a high-resolution and a high-speed camera to track the fracturing processes during the tests. The load, axial displacement, and time data were recorded for all the experiments, and the data collection was synchronized with the image frames from the high-resolution and high-speed cameras. This made it possible to conduct a comprehensive analysis of the specimens' behavior under uniaxial compression and fracture processes that occur during the tests.

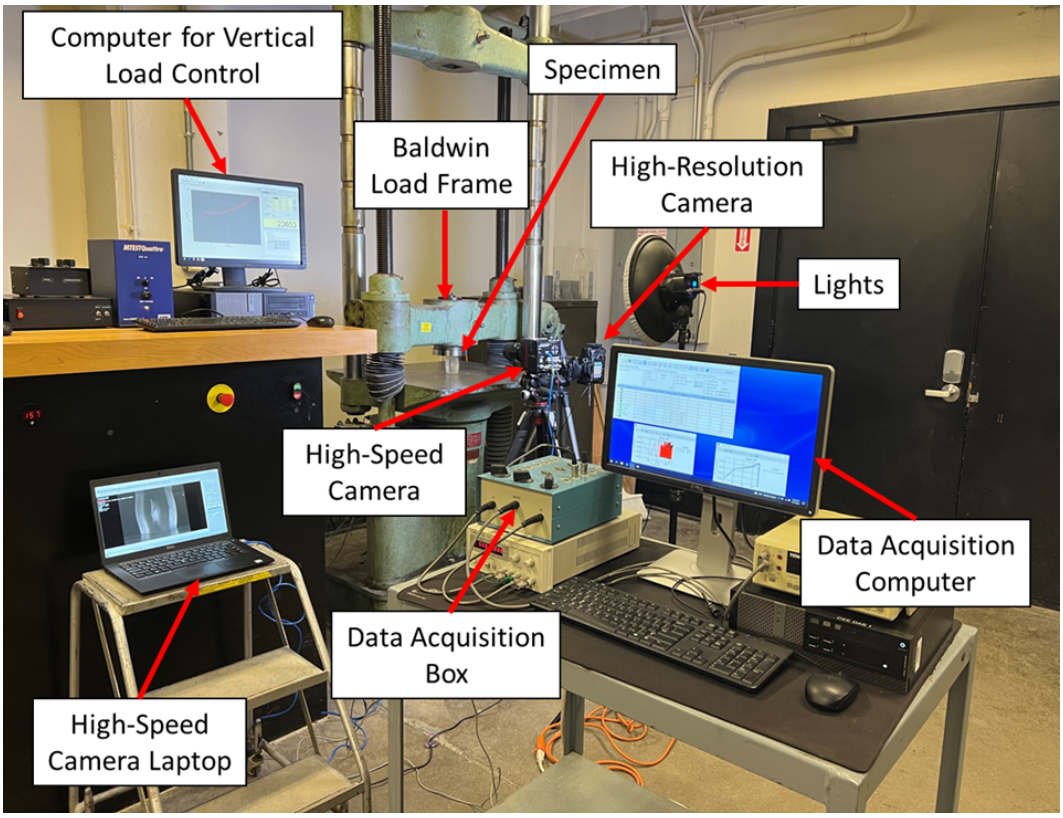

Figure 2-10: Photograph of the test setup showing the different equipment involved for uniaxial compression and data acquisition.

Both cameras were connected to a data acquisition system that facilitated the synchronization of the data (post-processing) with time against the stress and strain values obtained from the Baldwin load frame. This process of the cameras with the Baldwin load frame made it possible to accurately relate the images with their corresponding stress and strain values, resulting in a more comprehensive understanding of the test results. A schematic of the test setup depicting the cameras and the data acquisition system, along with the Baldwin load frame is shown in Figure 2-11.

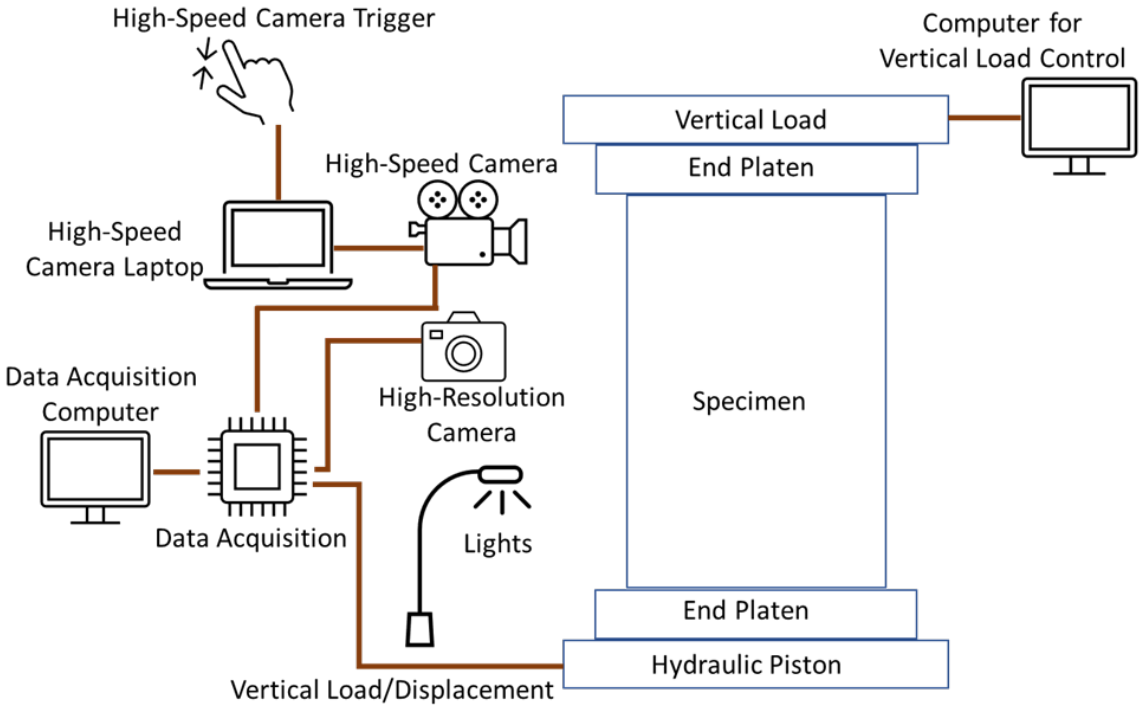

Figure 2-11: Uniaxial compression on prismatic specimen schematic. The central data acquisition saves vertical load and displacement data from load frame, as well as high-resolution and high-speed camera images, to relate observed events to stress-strain-time data.

2.4.1 Imaging Apparatus

As mentioned in the previous section, crack events were recorded using a high-resolution camera that takes images at 1 second intervals throughout the entire duration of the test and a high-speed camera capturing only 2.5 seconds of the test at a much faster rate of 5000 frames per second.

The high-resolution camera utilized in this study was the Sony alpha 7R III, shown in Figure 2-12. The Sony alpha 7R III is a mirrorless digital camera that features a 42.4-megapixel back-illuminated full-frame Exmor R BSI CMOS sensor. The camera has a resolution of 7952 x 5304 pixels and features a fast autofocus system with 399 phase-detection points. It is equipped with FE 2.8/90 MACRO G OSS lens. The aperture ranges from a minimum of F/22 to a maximum of f/2.8. This range allows the user to control the amount of light entering the camera and adjust the depth of field in the image. A smaller aperture (higher f-number) can create a greater depth of field, keeping more of the image in focus from foreground to background, while a larger aperture (lower f-number) can create a shallower depth of field, blurring the background and isolating the subject in the foreground. The minimum focal distance is 280 mm, and the fixed focal length is 90 mm.

Figure 2-12: Sony alpha 7R III high-resolution camera used during testing.

The primary function of this camera was to capture time-lapse images of the specimens, at an interval of 1 second, from the beginning of loading until failure of the specimen or the end of the test. This was essential, as it made it possible to capture key events that may occur in the specimen prior to failure such as the initiation of cracks, spalling, crack closure, and others. Having this camera makes it possible to observe events that would otherwise be missed by the high-speed camera.

The high-speed video camera used was a Photron FASTCAM Mini AX200 with a 105 mm Nikon macro lens, shown in Figure 2-13. This lens features a fast maximum aperture of f/2.8. The camera has a resolution of 1,024 x 1,024 pixel at up to 6,400 frames per second. The camera's ability to capture fast-moving events in high detail and provide slow-motion playback makes it a valuable tool for these types of tests. The settings of the camera, including the frame rate, resolution, shutter speed, and trigger partition of recorded data, can be adjusted by the user. Moreover, the advanced triggering capabilities make it possible to precisely control when recording starts and ends, making it ideal for capturing recordings of the significant events.

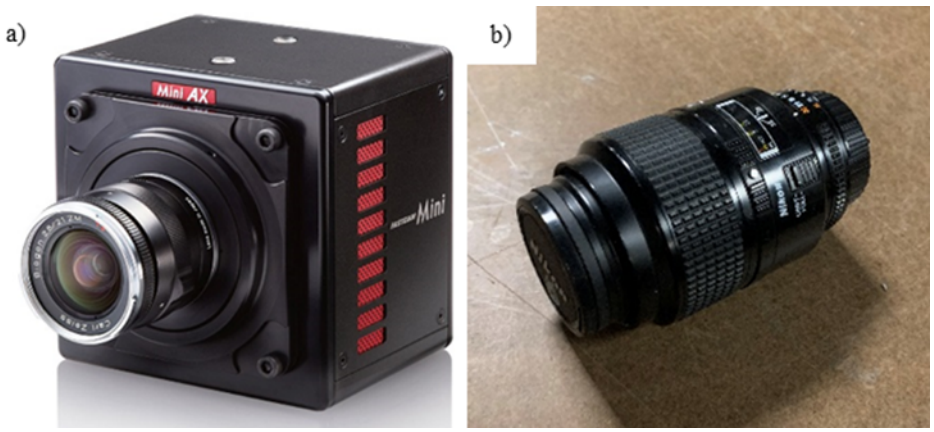

Figure 2-13: a) Photron FASTCAM Mini AX200 high-speed camera used during testing, b) 105 mm Nikon macro lens used during testing.

The manual triggering of the high-speed video camera was facilitated through the laptop that controlled the device. The camera was in constant recording mode, and upon manual activation of the trigger, the preceding few seconds of high-speed footage was stored for analysis. Additionally, the camera was equipped with a post-trigger setting, which allowed the user to specify the number of frames to be captured after the camera has been triggered. This event-triggered approach made it possible to capture detailed and high-speed images of any sudden changes in the specimen, providing valuable insights into the fracture behavior.

To obtain optimal lighting conditions for the test imaging, a round 14.5 inches Genaray Spectro LED flood light was utilized. The device, depicted in Figure 2-14, is equipped with high-intensity LED lights and features a beam angle of 120 degrees and a color rendering index (CRI) of 96, with a color temperature of 5600K. This configuration of the Spectro LED flood light ensured a bright and evenly illuminated surface on the test specimen.

Figure 2-14: Spectro LED flood light used during testing.

2.4.2 Data Collection and Synchronization

Three main data sources were utilized to gather information about the specimens during the experiments. These sources were the Baldwin load frame, the high-resolution camera, and the high-speed camera. During testing, all three sources were connected to a central data acquisition system, which was responsible for time data synchronization. The aim of the time data synchronization is to relate the time, load, and axial displacement data recorded from the Baldwin load frame with the high-resolution images and high-speed video. This is important to identify the key frames' time of occurrence. Moreover, this makes it possible to match the frames from the two cameras with the stress-strain-time data to within fractions of a second.

The data from the high-resolution and high-speed cameras provides insight into the fracturing processes as well as the observed deformation and specimen behavior while being subjected to loading. Analysis of the frames enables the identification of crack initiation, propagation, and coalescence. For this particular type of material, where cracking and related events take place over a longer period of time than can be saved on the high-speed camera due to the limitations of its internal memory, the high-resolution images are very helpful. Having the frames from both cameras allows us to compare how the deformations and specimen properties changed from the start of the test through the very end, while capturing the intricate details of key events.

2.5 Test Program

The testing program consisted of a seating stage in which the specimens were preloaded to a target of 100 lbs at a rate of 0.1 inches per minute (in/min). This step was crucial to ensure the specimens were in contact with the loading platen and under a compressive load before the main testing phase. This also minimizes any potential errors that may arise due to improper contact between the specimen and platen. After the seating stage, the specimens were loaded at a specified rate, as detailed in Chapter 3, until the end of the test. The Baldwin load frame has a maximum capacity of 60 kips and was programmed to stop the test once the load capacity was reached or when a 2% load drop was detected. The test was manually stopped in cases where a significant amount of crack propagation occurred to avoid specimen failure and to preserve the specimen, when possible. A load vs. time plot detailing the preloading, testing, and stopping phases as programmed in the experiments is shown in Figure 2-15.

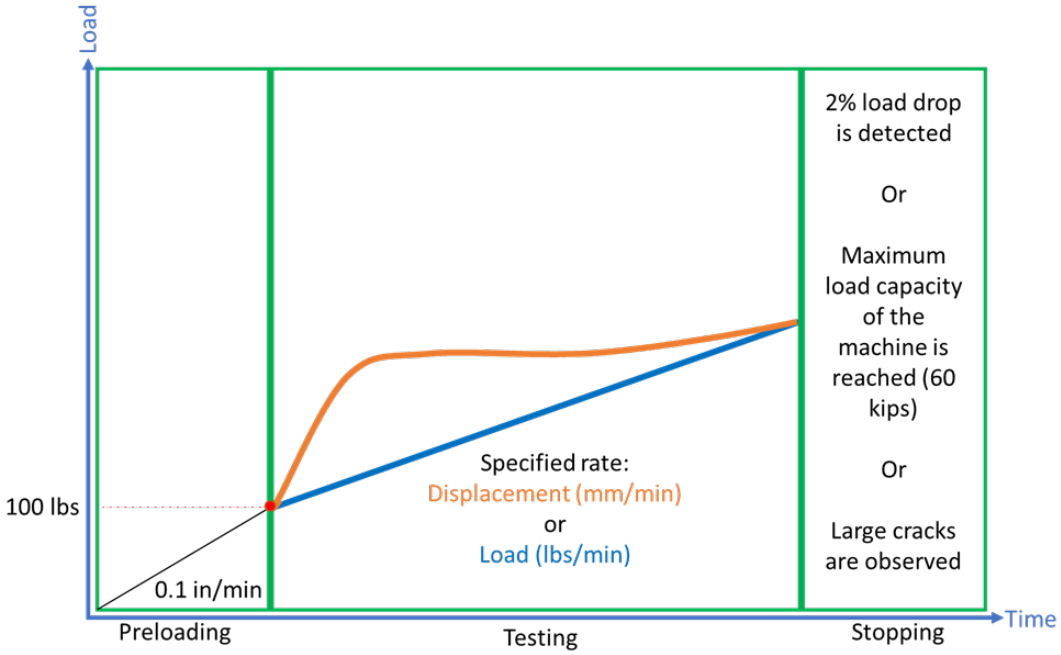

Figure 2-15: Load versus time plot that depicts the preloading, testing, and stopping phases as programmed in the experiments.

Chapter 3

Results and Discussion

3.1 Introduction

In this chapter, the investigated parameters are discussed in detail. The results are presented in the form of true stress plotted against strain for the uniaxial experiments. The true stress is determined by dividing the load by the instantaneous cross-sectional area. Relevant parameters such as yield stress and ultimate compressive stress are also compared. Yield stress is defined as the value above which the material begins to deform plastically and was determined using the 0.2% offset method. This method involves constructing a line parallel to the initial (linear) portion of the stress-strain curve but offset by 0.2% from the origin on the strain axis and identifying the point of intersection with the curve. More details on this method can be found in Appendix A. Ultimate compressive stress was defined as the peak stress recorded. Visual observations of the specimens throughout the tests are also discussed. An example stress-strain plot is shown in Figure 3-1 demonstrating the locations of the yield stress and ultimate compressive stress.

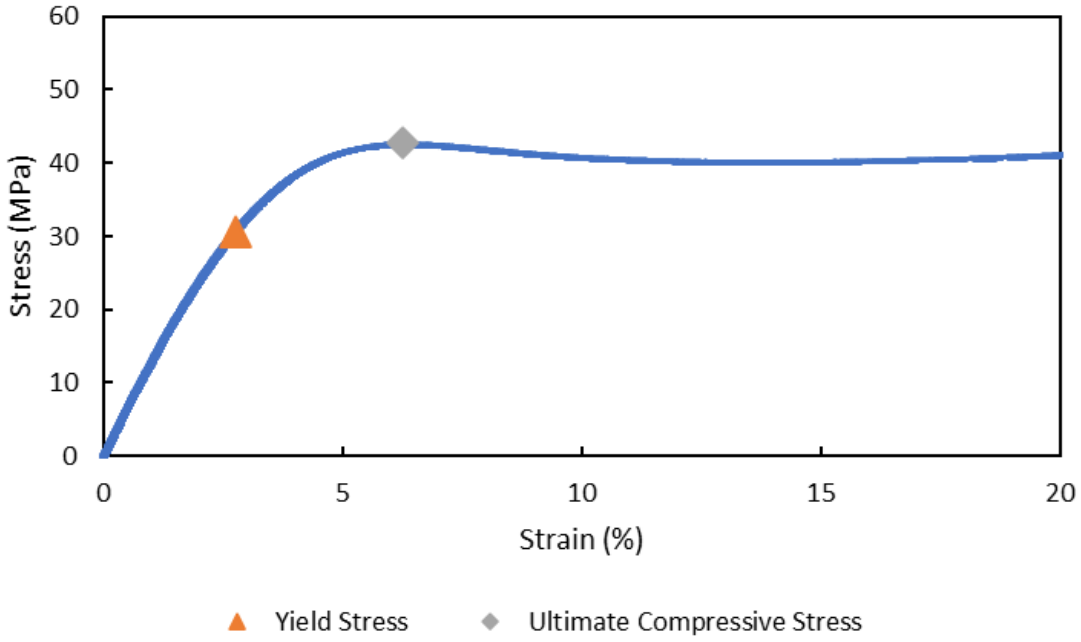

Figure 3-1: Example stress-strain curve for specimen subjected to uniaxial loading with yield stress (orange triangle) and ultimate compressive stress (grey diamond) markers.

The following four main sections (3.2 - 3.5) are divided into: process parameters, equipment and testing conditions, specimen parameters, and boundary conditions (e.g., frictional end effects), respectively. It is worth noting that the investigations in these sections were designed based on previous observations from initial tests, and hence were all conducted in parallel. The findings of these investigations build into Section 3.6, which compares the fracturing behavior of specimens containing internal flaws and specimens containing thorughgoing flaws at various flaw inclinations.

3.2 Process Parameters

In this section, two process parameters are investigated: post-processing curing and printing orientation relative to the build platform. Post-processing curing refers to exposing a specimen to UV light after printing is complete and the supports are removed, with the purpose of promoting polymerization and altering the mechanical properties of the specimen. Printing orientation, on the other hand, refers to how the 3D model is positioned on the build platform during the printing process.

3.2.1 Post-Processing Curing

In Stereolithography (SLA) printing, a light source is used to cure a photosensitive resin containing a photoinitiator. As described in Chapter 2, the curing process solidifies the resin in a layer-by-layer manner to create the 3D object.

The initial polymerization process by the printer laser provides solid specimens with adequate handling strength; however, past research suggests that a printed part can be further enhanced. Depending on the resin material, a UV flood (e.g., uniform and widespread exposure) post-processing curing step may be included to raise the degree of polymerization and improve the mechanical properties of the final product. During printing, fast curing monomers and short irradiation exposures can trap a significant amount of residual initiator. The trapped initiators can be used for post-processing curing in a UV chamber, as shown in Figure 3-2, to promote the completion of binding reactions.

Figure 3-2: Form Cure UV chamber used for post-processing curing of specimens.

The mechanical properties of the final product are heavily influenced by the post-processing curing treatment and the wavelength of the light source. For commercial resins containing acrylates and methacrylates, a wavelength of 405 nm has been frequently used for both printing and post-processing curing. Heat deflection temperature is the temperature at which a material will start to deform. Since the heat deflection temperature under load varies from about 75°C for low molecular weight to 100°C for high molecular weight methacrylates, most industrial post-processing curing is performed at an intermediate temperature of approximately 60°C.

The effect of post-processing curing was investigated by conducting uniaxial tests on three identical prismatic specimens with dimensions (3 in x 1.5 in x 1.5 in). The first specimen was tested in a green state, which means it was not placed in the UV chamber after printing. The remaining two specimens were both post-processing cured at a temperature of 60°C for 15 and 30 minutes, respectively. Figure 3-3 shows the stress-strain data for the three tests at a displacement-controlled loading rate of 1 mm/min.

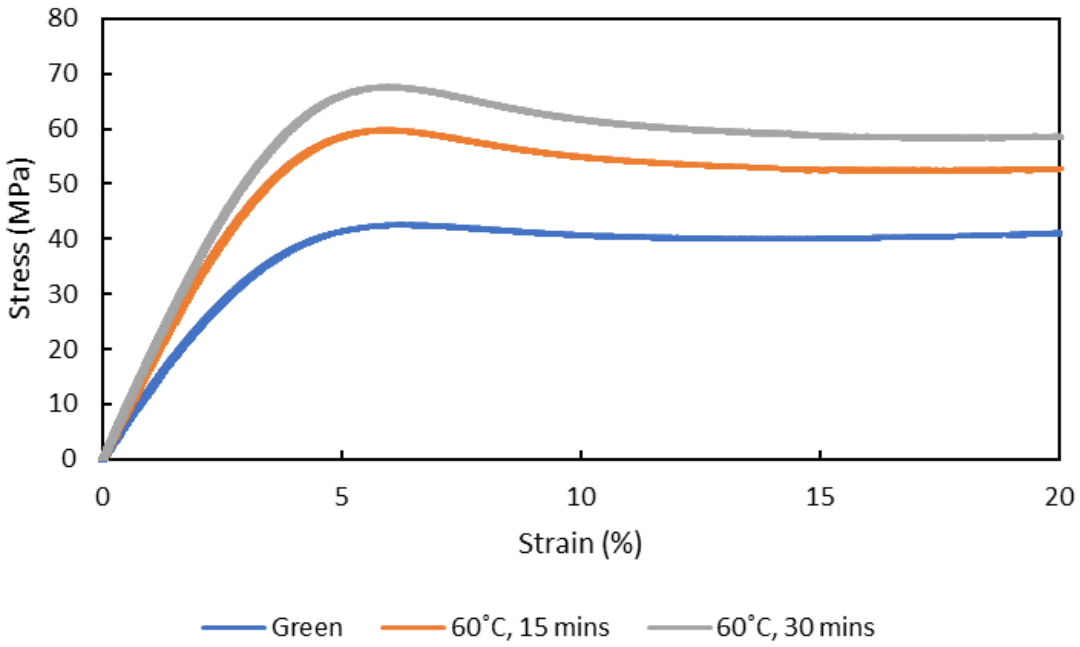

Figure 3-3: Stress-strain data comparing specimens with different post-processing curing settings subjected to uniaxial loading.

The yield stress and ultimate compressive stress values were determined from the stress-strain plots and are shown below in Figure 3-4.

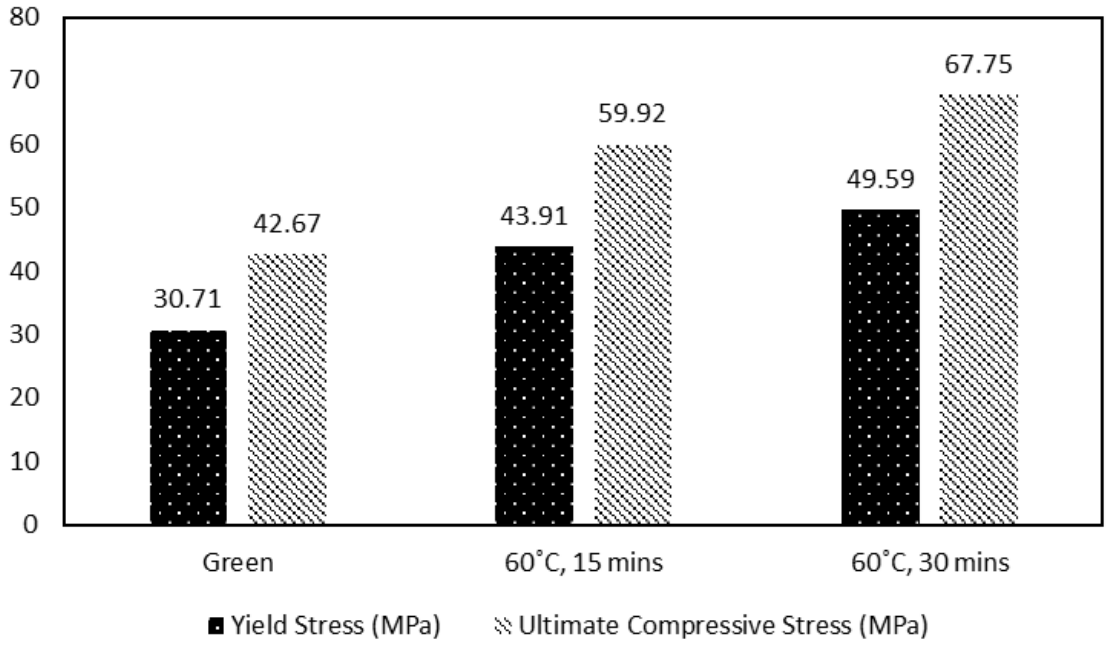

Figure 3-4: Yield stress and ultimate compressive stress values for specimens with different post-processing curing settings subjected to uniaxial loading.

The results clearly show a difference in the yield stress and ultimate compressive stress values. The trend was as expected in that post-processing curing increases the strength of the material. Also, as the post-processing curing time increased, the strength of the material increased. Though, the difference between the two post-processing cured specimens was comparatively smaller.

As evidenced by the stress-strain curves of these tests, the specimens that were post-processing cured had higher yield stress and ultimate compressive stress values. This is an indication of an increase in brittleness. This was also observed in the visual images taken during the tests. Accordingly, the two specimens that were post-processing cured had fractures developing sooner and experienced less deformation compared to the specimen tested in the green state. A series of image frames of the three specimens taken at three time intervals: start of the test (labeled $t_{initial}$), middle of the test (labeled $t_{intermediate}$), and end of the test (labeled t_{final}) along with corresponding sketches are shown in Figure 3-5.

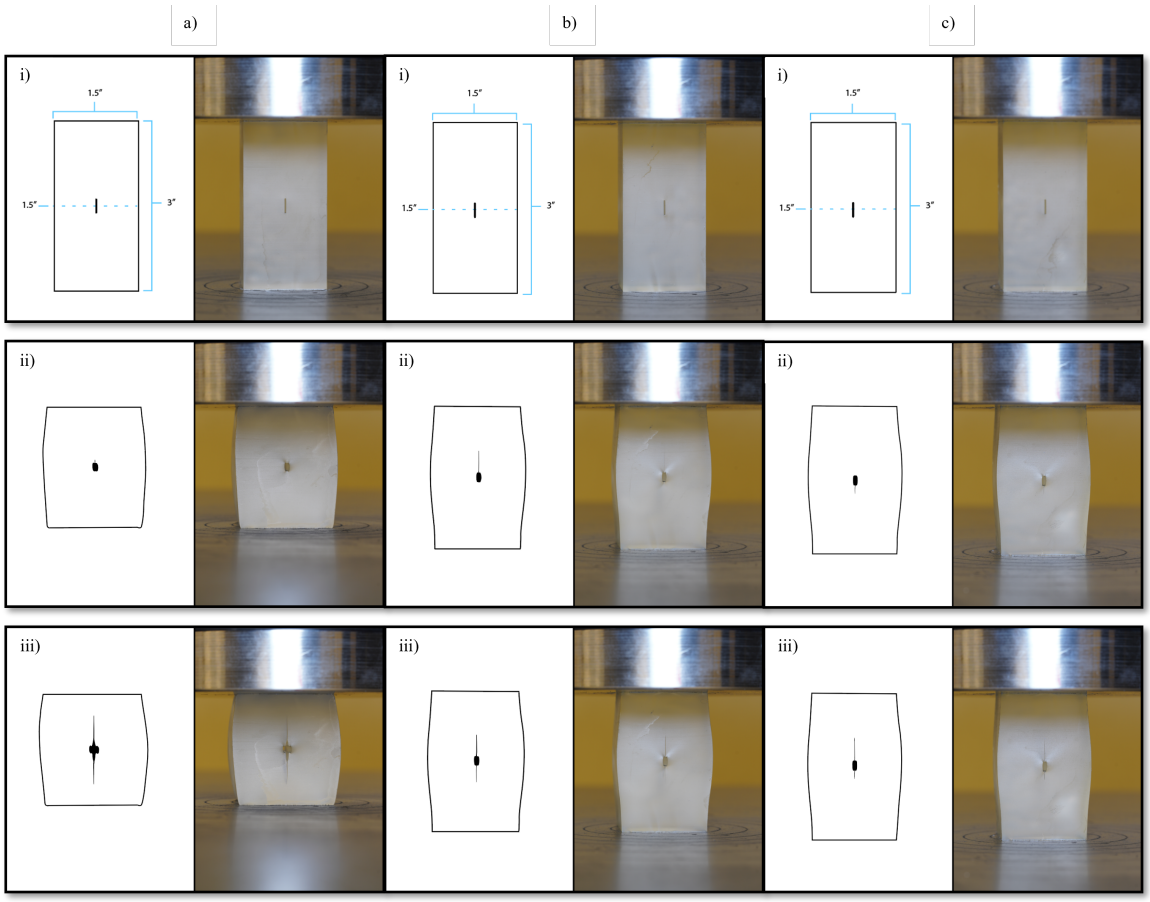

Figure 3-5: Sketch alongside image frame of specimens with different post-processing curing settings subjected to uniaxial loading at different times: a) Green, b) 60°C, 15 mins, c) 60°C, 30 mins, i) $t_{initial}$, ii) $t_{intermediate}$, and iii) t_{final}.

The specimens were tested in a green state (no post-processing curing) for the rest of the experiments in this study. This decision was made out of concerns about the depth (and thus uniformity) of the post-processing curing given the size of the specimens. Suggestions about investigating this are presented in Chapter 4, Section 2 (Future work).

3.2.2 Printing Orientation

Printing orientation refers to how the 3D model is positioned on the build platform during the printing process, which in turn dictates the direction of the layers being printed. This factor significantly impacts the accuracy, surface quality, and mechanical properties of the printed specimen. Appropriate orientation minimizes the need for support structures, reduces the number of layers printed, and ensures an optimal distribution of mechanical stresses. Moreover, optimal orientation can also enhance the transparency of the clear resin, which is crucial for observing and analyzing internal structures and features.

This study focused on three printing orientations, which are shown in Figure 3-6. The first orientation has the longitudinal axis of the specimen oriented parallel to the build platform (parallel). The second orientation has the the longitudinal axis oriented 45° to the build platform (inclined). The third orientation has the longitudinal axis oriented perpendicular to the build platform (perpendicular).

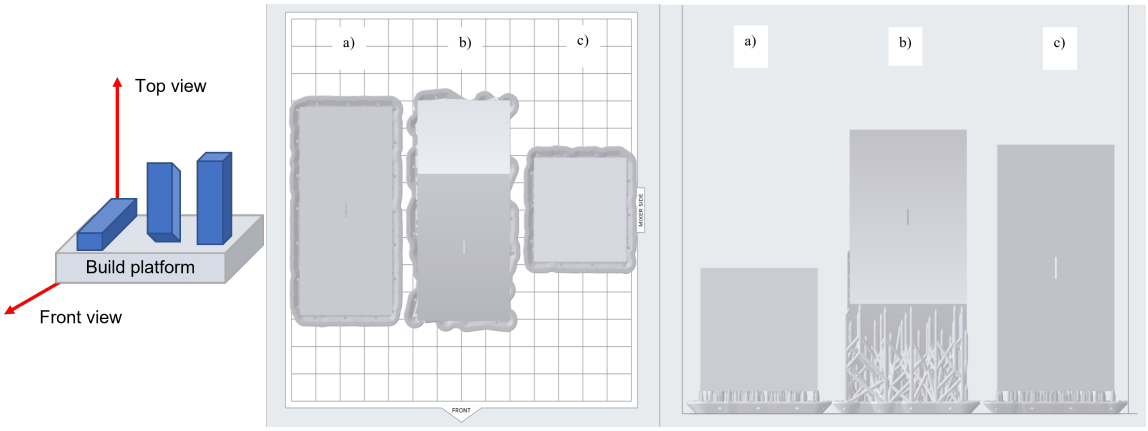

Figure 3-6: Screenshots from Preform software of top view (left) and front view (right) illustrating the different specimen print orientations on the build platform, where: a) 0° (parallel), b) 45° (inclined), and c) 90° (perpendicular).

The effect of printing orientation was investigated by conducting uniaxial tests on three identical prismatic specimens with dimensions (3 in x 1.5 in x 1.5 in). Each specimen was printed at a different orientation, which were at 0° (parallel), 45° (inclined), and 90° (perpendicular) to the build platform. Figure 3-7 shows the stress-strain data for the three tests at a displacement-controlled loading rate of 1 mm/min.

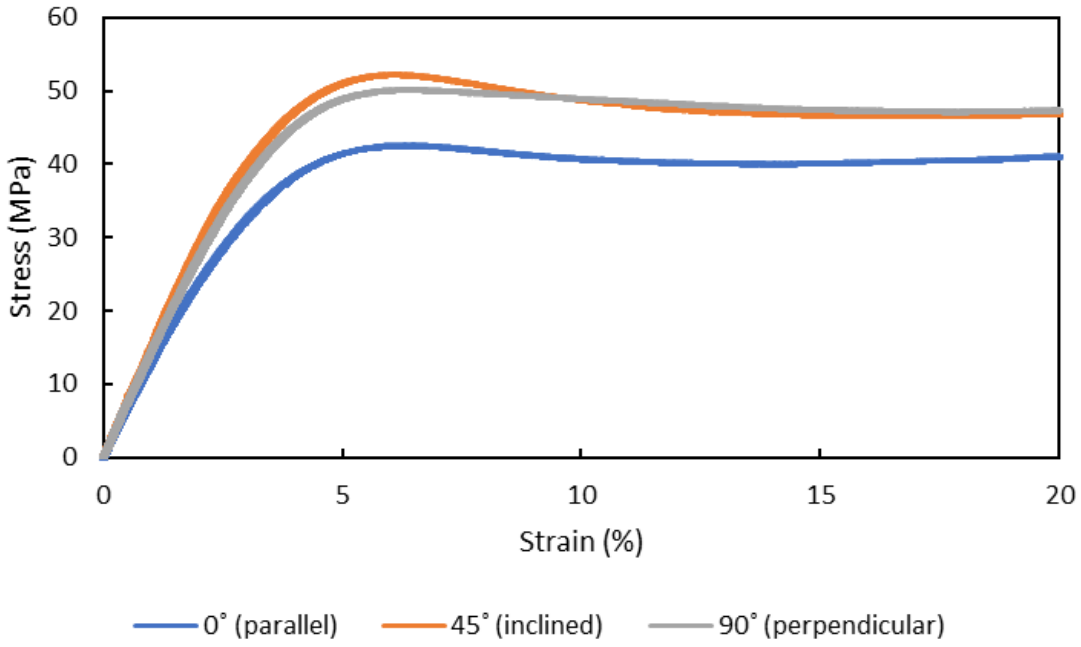

Figure 3-7: Stress-strain data comparing specimens printed at different orientations subjected to uniaxial loading.

The yield stress and ultimate compressive stress values were determined from the stress-strain plots and are shown below in Figure 3-8.

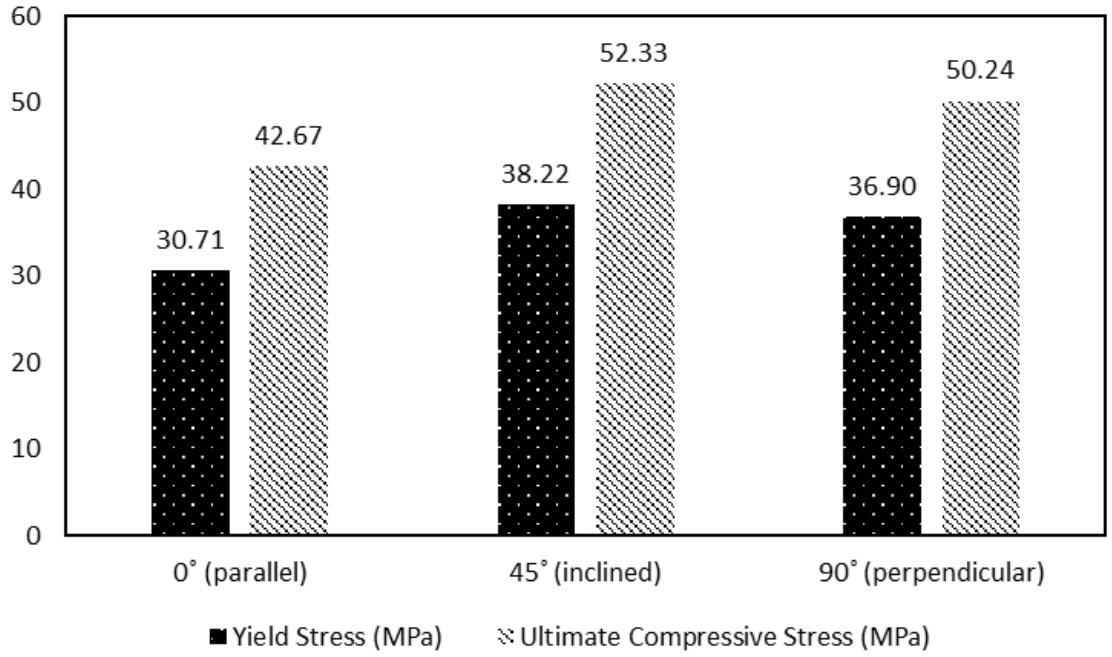

Figure 3-8: Yield stress and ultimate compressive stress values for specimens with different printing orientations subjected to uniaxial loading.

The results show that the different printing orientations exhibit varying strength. The specimen printed at 45° (inclined) had the highest yield stress and ultimate compressive stress values, followed by the specimen printed at 90° (perpendicular), then the specimen printed at 0° (parallel). It is likely that the specimen printed at 0° (parallel) has the lowest strength because the layer laminations are arranged perpendicular to the major compressive force.

It was observed during the tests that the specimen printed at 0° (parallel) experienced less bulging, more uniform deformation, and more stable crack propagation compared to the other printing orientations. A series of image frames of the three specimens taken at three time intervals: start of the test (labeled $t_{initial}$), middle of the test (labeled $t_{intermediate}$), and end of the test (labeled t_{final}) along with corresponding sketches are shown in Figure 3-9.

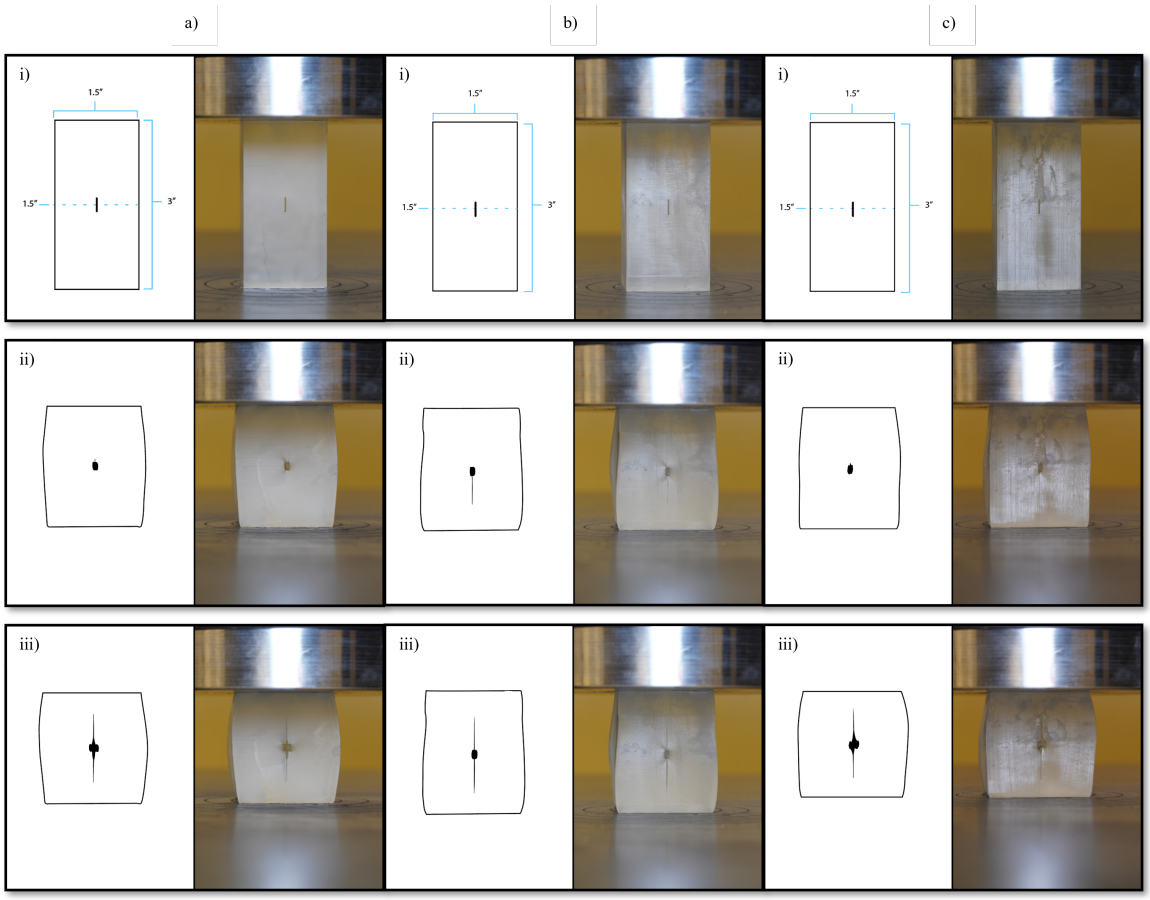

Figure 3-9: Sketch alongside image frame of specimens with different printing orientations subjected to uniaxial loading at different times: a) 0° (parallel), b) 45° (inclined), c) 90° (perpendicular), i) $t_{initial}$, ii) $t_{intermediate}$, and iii) t_{final}.

The specimens were printed at 0° (longitudinal axis parallel to the printing platform) for the rest of the experiments in this study. As mentioned, the specimen tested with this print orientation experienced less bulging, more uniform deformation, and more stable crack propagation. In addition, some degredation in surface quality was noticed for the specimens printed at 45° (inclined) and 90° (perpendicular), making it harder to observe the internal features of the specimen.

3.3 Equipment and Testing Conditions

In this section, several conditions related to the equipment and test set up are investigated. Moreover, these are: type of compression platen used, centering of the specimen, loading control method, and the rate at which loading is applied. Ensuring that these conditions are adequate and consistent is essential for obtaining reliable and meaningful results.

3.3.1 Compression Platen and Centering

Compression platens are flat plates or disks used to apply a compressive force on a specimen. There are many types available, with the two main types being spherically seated (flexible) and fixed platens. An image of these platens is shown in Figure 3-10.

Figure 3-10: Photograph of flexible (left) and fixed (right) compression platens.

Using a flexible platen helps a specimen self-align during compression testing and is required for many ASTM tests for different materials including concrete and wood. However, from initial experiments conducted, it was noticed that the plate tilts at high loads. This leads the specimen to experience uneven loading and buckling, which eventually causes the specimen to burst in failure. It was found that the cause of this behavior could be due to uncentering, the specimen not being perfectly aligned with the compression platen before starting the test. To address this, an acrylic centering template was fabricated to ensure the proper centering of the specimen.

A high-power laser beam was utilized to accurately cut a circular, 0.5-inch thick, centering template from acrylic material with a diameter similar to that of the compression platen. A hole in the middle with dimensions equivalent to the base of the specimen to be tested was also included. The use of laser cutting technology allowed for precise and efficient fabrication of the centering template. A side view schematic and top view image of the centering template is shown in Figure 3-11.

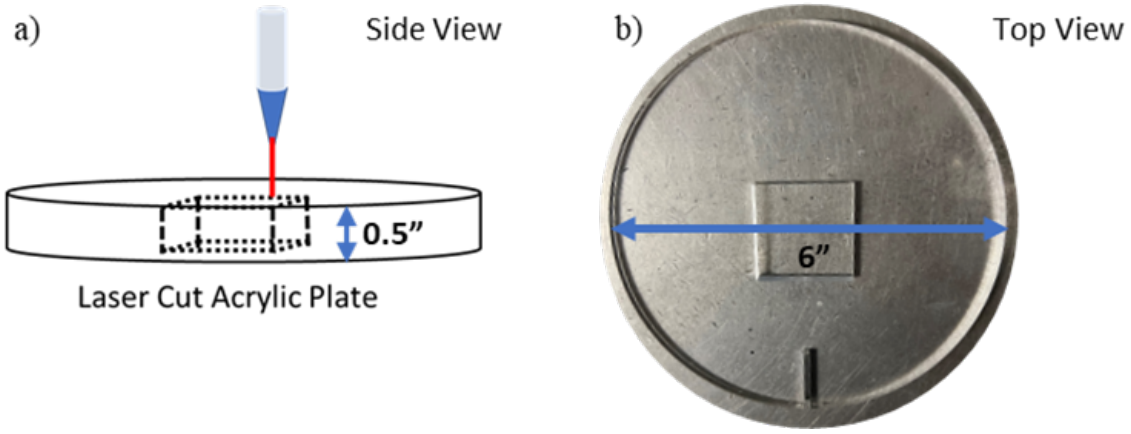

Figure 3-11: a) Side view schematic of centering template and b) top view photograph of the centering template used to align the specimens before testing.

The centering template is placed before the experiment as shown in Figure 3-12. It is important to note that the centering template is removed by raising the load frame before the test is started.

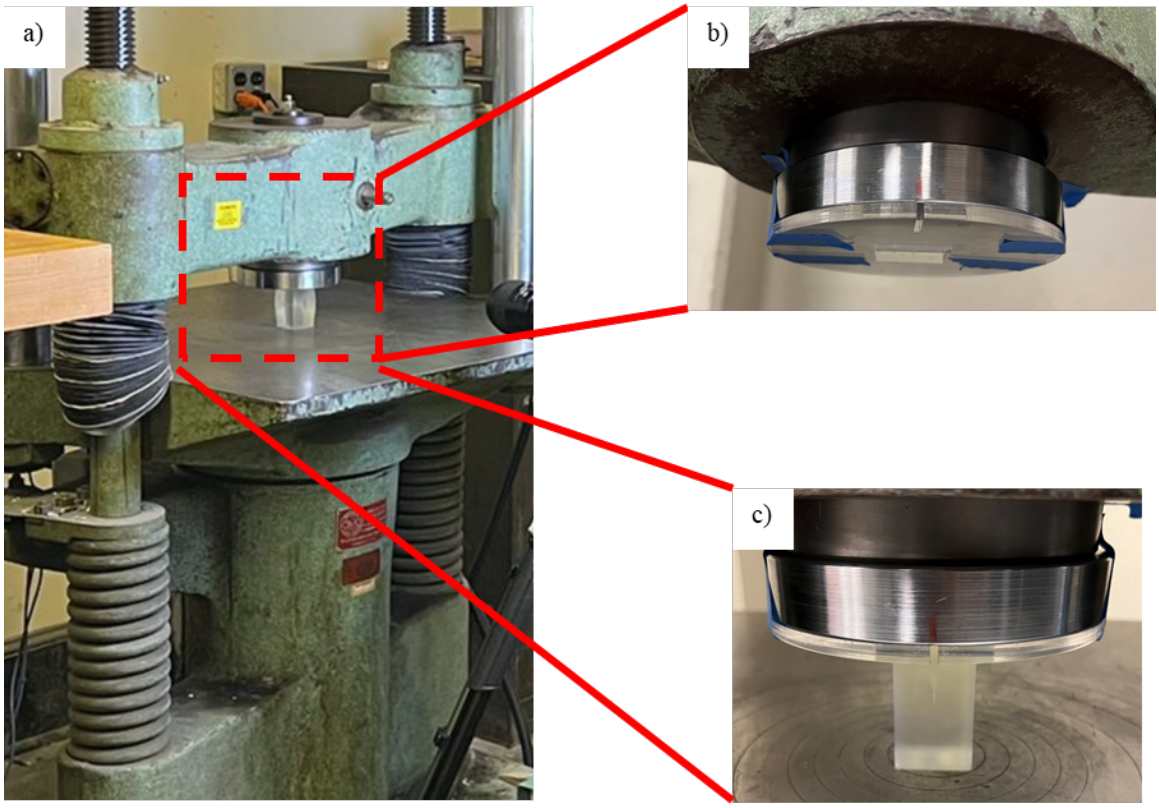

Figure 3-12: a) Overview photograph of centered specimen under uniaxial load, b) close-up view of centering template placed on the compression platen, and c) specimen aligned using the centering template.

The effect of compression platen type and the specimen centering was investigated by conducting uniaxial tests on four identical prismatic specimens with dimensions (3 in x 1.5 in x 1.5 in). For each compression platen type - fixed and flexible - tests were conducted on both a centered and an uncentered specimen. Figure 3-13 shows the stress-strain data for the four tests at a displacement-controlled loading rate of 1 mm/min.

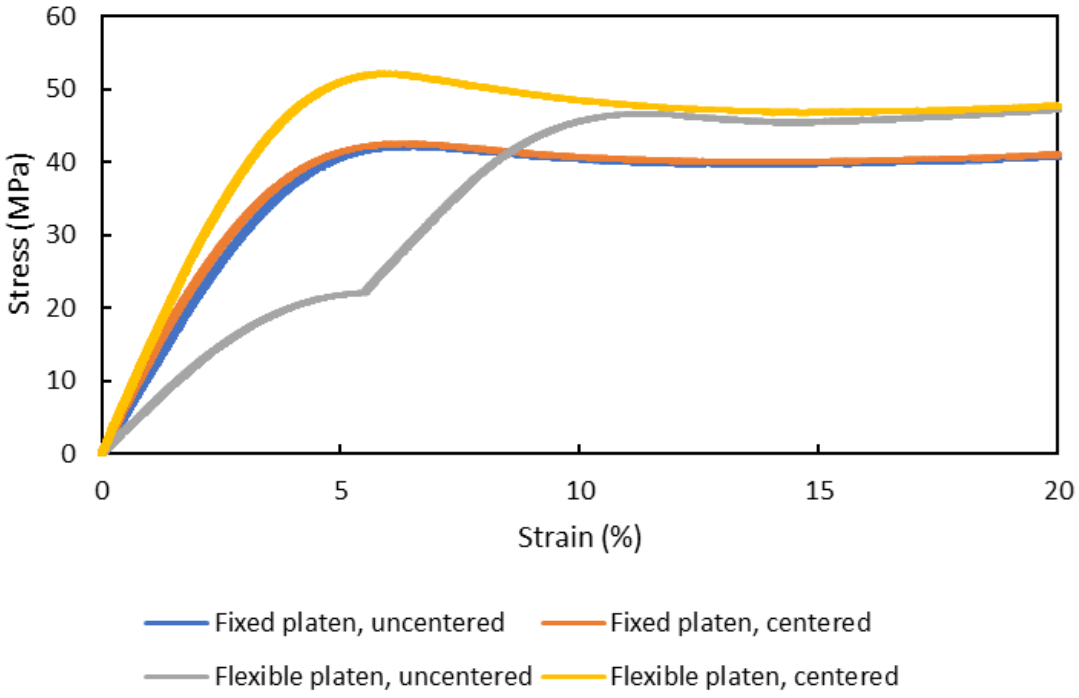

Figure 3-13: Stress-strain data comparing specimens subjected to uniaxial loading with different compression platen types and specimen centering.

The yield stress and ultimate compressive stress values were determined from the stress-strain plots and are shown below in Figure 3-14.

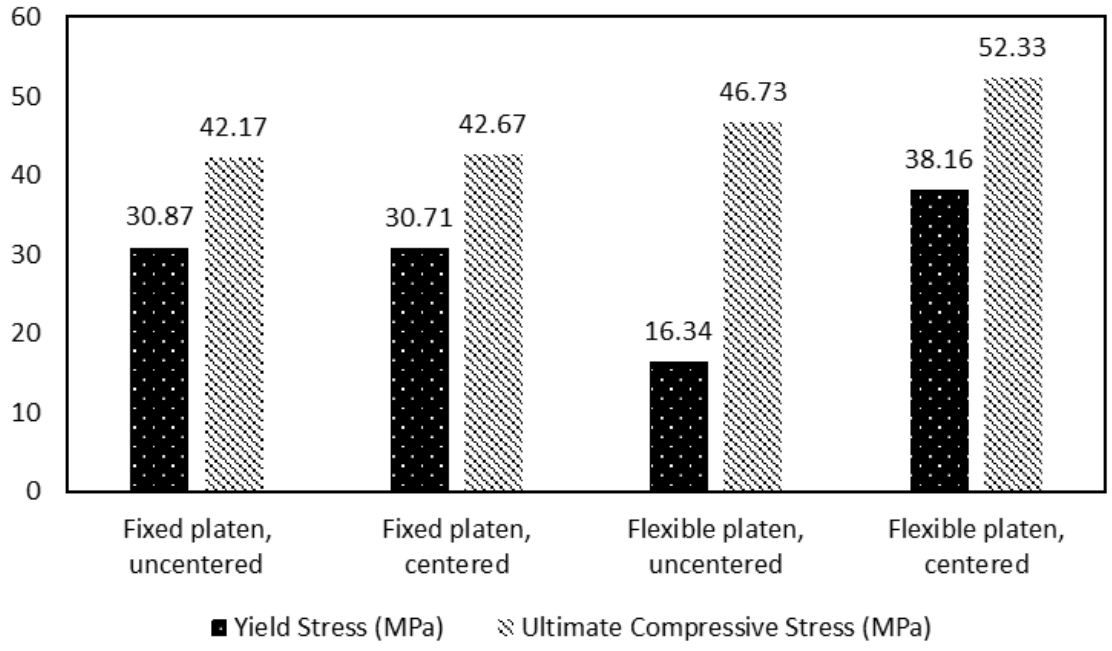

Figure 3-14: Yield stress and ultimate compressive stress values for specimens subjected to uniaxial loading with different compression platen types and specimen centering.

Evidently, little difference exists in the mechanical properties between the specimens tested with the fixed compression platen regardless of centering. However, it was observed that the specimen that was not centered experienced more bulging, which could lead to eventual buckling and explosion at higher loading. Images of the specimens subjected to uniaxial loading with the fixed compression platen are shown in Figure 3-15.

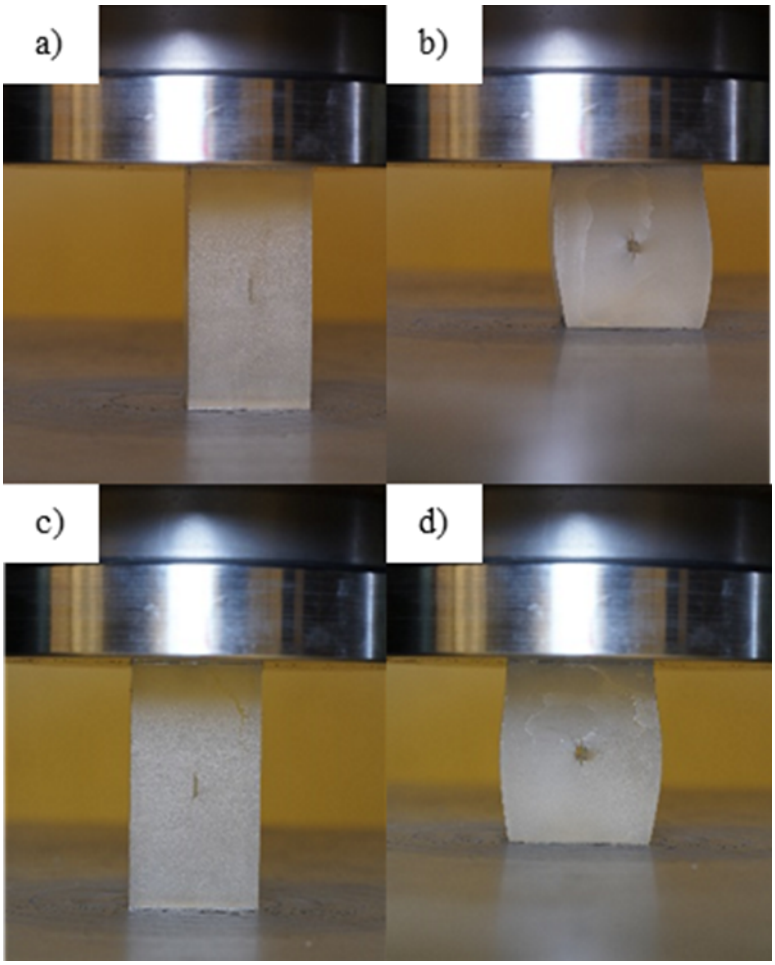

Figure 3-15: Frames of specimens subjected to uniaxial loading using the fixed compression platen. Uncentered specimen: a) low loading and b) high loading. Centered specimen: c) low loading and d) high loading.

For the flexible compression platen tests, the uncentered specimen clearly experienced unequal distribution of load which caused it to deform on one side more than the other. This effect was more visually apparent at higher loads but still present from the beginning of the test. Images of the specimens subjected to uniaxial loading with the flexible compression platen are shown in Figure 3-16.

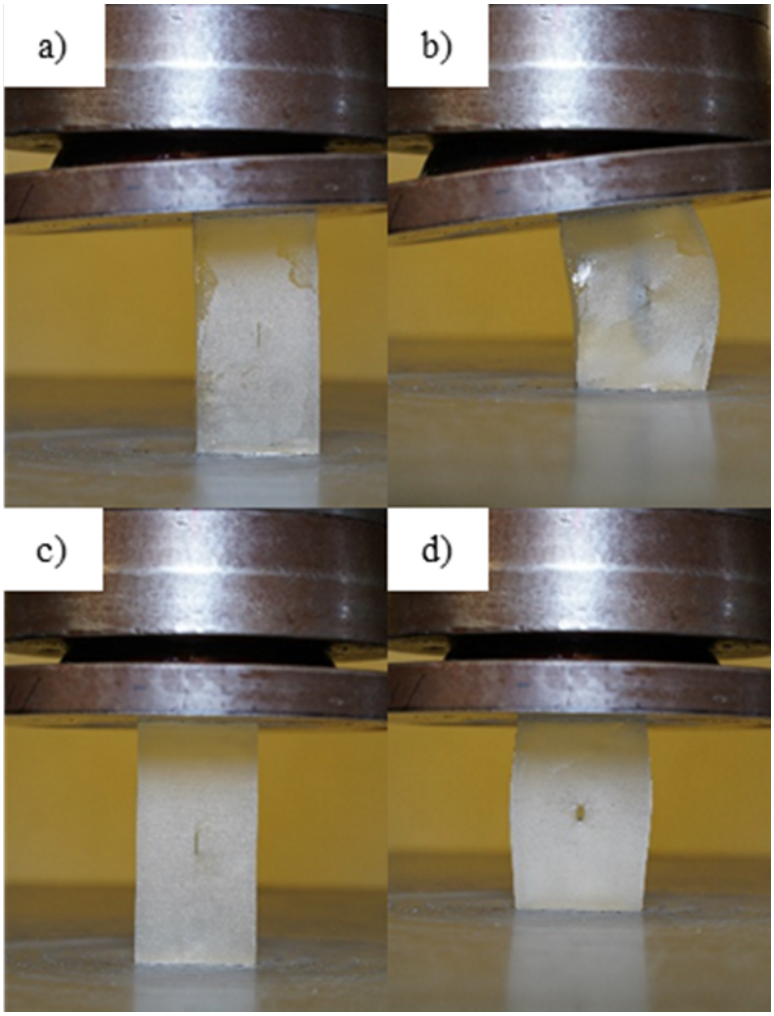

Figure 3-16: Frames of specimens subjected to uniaxial loading using the flexible compression platen. Uncentered specimen: a) low loading and b) high loading. Centered specimen: c) low loading and d) high loading.

The fixed compression platen along with the centering template were used for the rest of the experiments in this study. This was done to maintain consistency for reliable comparison in the tests.

3.3.2 Loading Control and Rate

Two of the most common loading control methods are displacement-controlled (mm/min) and load-controlled (lb/min). There is no set loading control method and rate for uniaxial compression tests, but recommendations and suggestions exist (Isah et al., 2020; ISRM, 2007; ASTM, 2014) based on the time to failure and the size of the specimen. This can be problematic because different rocks behave differently under loading.

The effect of the loading control method and rate was investigated by conducting uniaxial tests on six identical prismatic specimens with dimensions (3 in x 1.5 in x 1.5 in). Figure 3-17 shows the stress-strain data for the six tests at displacement-controlled and load-controlled loadings at different rates.

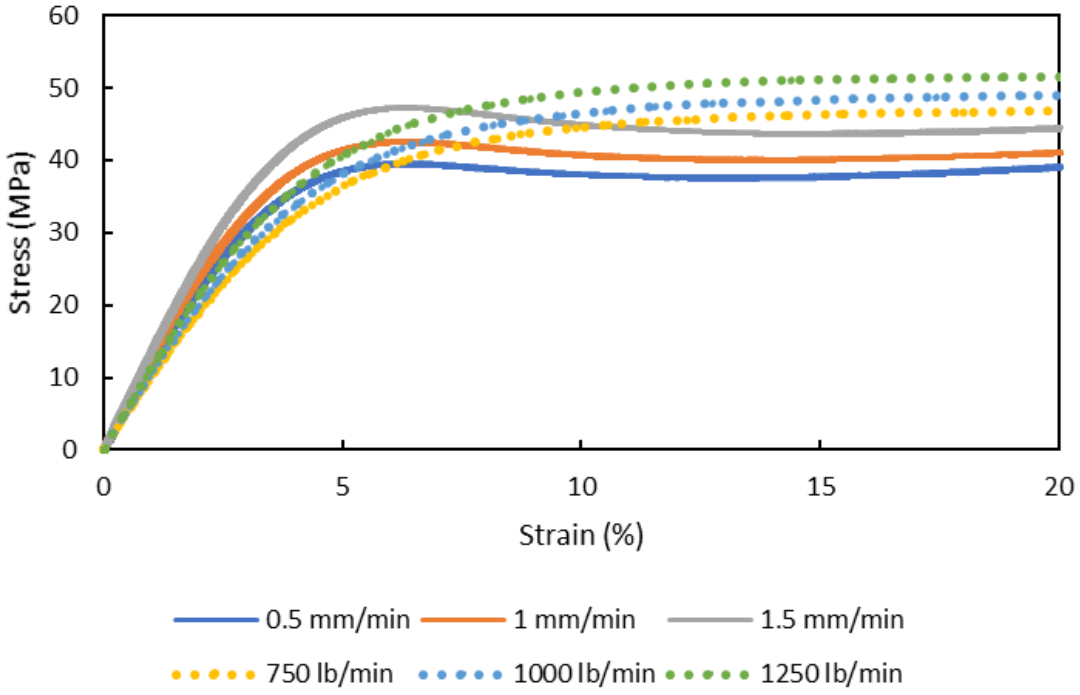

Figure 3-17: Stress-strain data comparing specimens subjected to uniaxial loading at different displacement (solid curves) and loading (dotted curves) rates.

The yield stress and ultimate compressive stress values were determined from the stress-strain plots and are shown in Figure 3-18. There are no ultimate compressive stress values for the specimens tested with load control because the material did not exhibit strain softening and thus no peak stress could be determined.

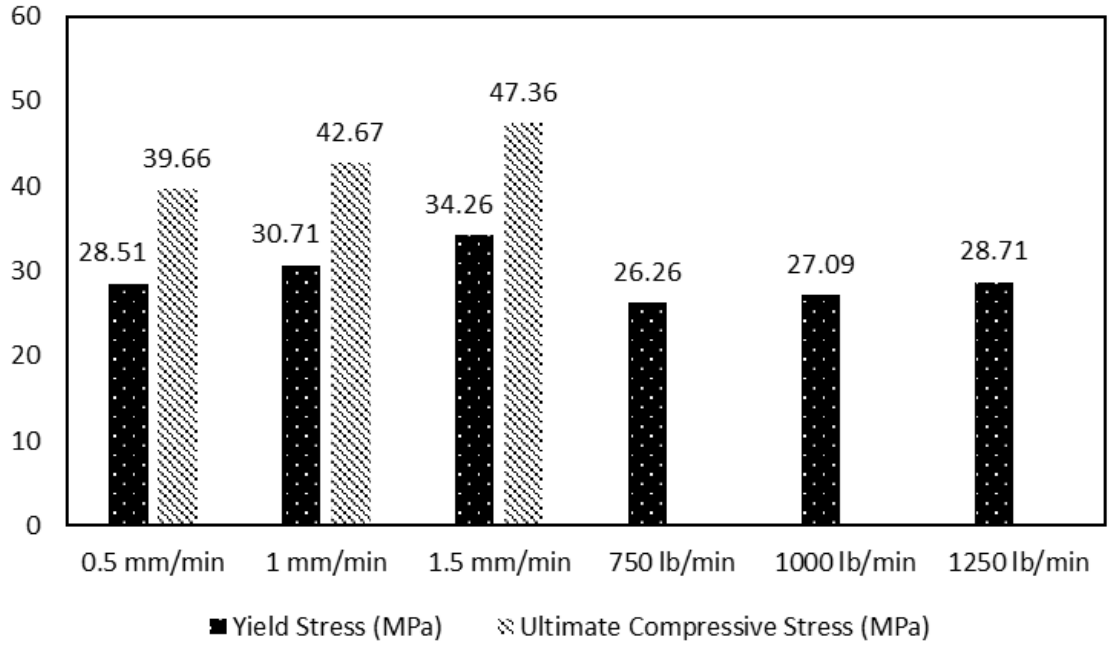

Figure 3-18: Yield stress and ultimate compressive stress values for specimens subjected to uniaxial loading at different displacement and loading rates.

The results above agree with the literature (Komurlu, 2018), indicating that the mechanical properties of rocks depend on the loading control method and rate applied. It is evident that the increase in rate increases the yield stress and ultimate compressive stress values (where applicable). For the load control method, strain increased slowly in the beginning (small stress) of the test but increased rapidly at higher stress. Displacement-based loading was more controlled and produced more stable fractures (e.g., cracks that steadily increase in length without any sudden jumps or branching). Hence, it was used for the rest of the experiments in this study at a rate of 1 mm/min.

3.4 Specimen Parameters

In this section, two specimen parameters are investigated: size and base geometry. The size effect refers to the phenomenon where the mechanical properties of a material may vary depending on the dimensions of the tested specimen. Base geometry in this context refers to the cross-sectional geometry of the specimen, which is related to the slenderness (a term used to describe the relation between the height and the smallest lateral dimension).

3.4.1 Size Effect

The influence of specimen size on the strength of materials has been discussed for years (Baecher and Einstein, 1981). The main conclusion of various theoretical models and experiments is that strength decreases with increasing volume. The size effect is explained by two theories. The first is based on statistical probability (extreme value theory): larger volumes are more likely to contain local weak spots and consequently larger specimens would fail at lower stresses compared to smaller specimens (Weibull, 1939). The second is stored strain energy theory, in which the total stored elastic energy in a specimen increases with its size (Glucklich and Cohen, 1968). Thus, a volume increase causes greater energy release, which reduces the strength.

The effect of specimen size was investigated by conducting uniaxial tests on three prismatic specimens with different sizes. The specimens varied, from a small size (2 in x 1 in x 1 in), followed by a medium size (3 in x 1.5 in x1.5 in), to a large size of (4 in x 2 in x 2 in). Figure 3-19 shows the stress-strain data for the three tests at a displacement-controlled loading rate of 1 mm/min.

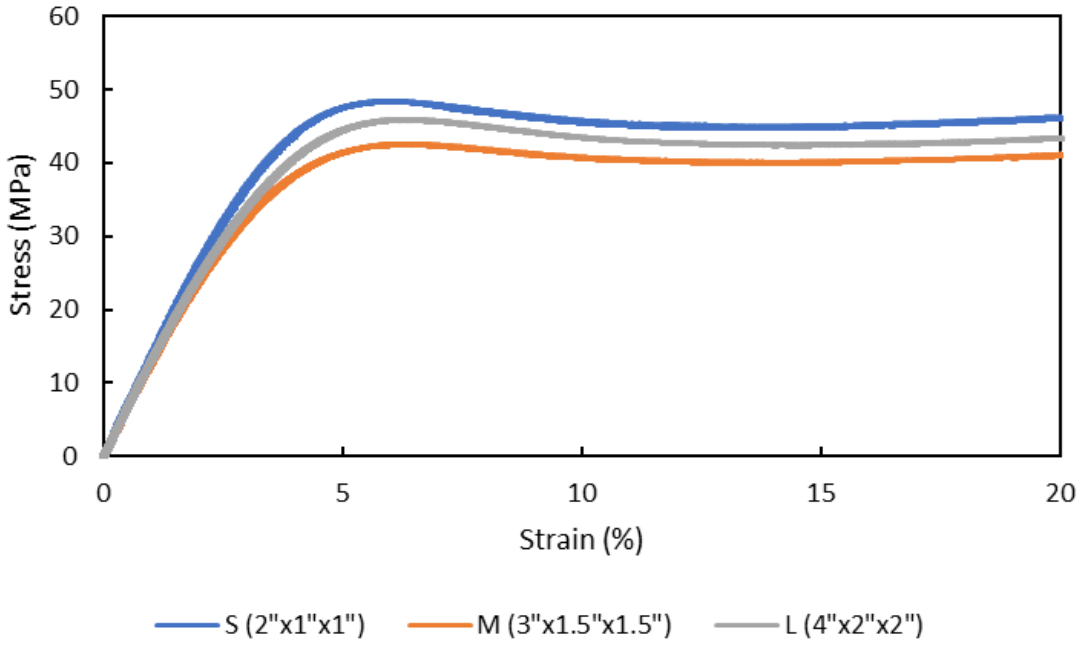

Figure 3-19: Stress-strain data comparing different size specimens subjected to uniaxial loading.

The yield stress and ultimate compressive stress values were determined from the stress-strain plots and are shown below in Figure 3-20.

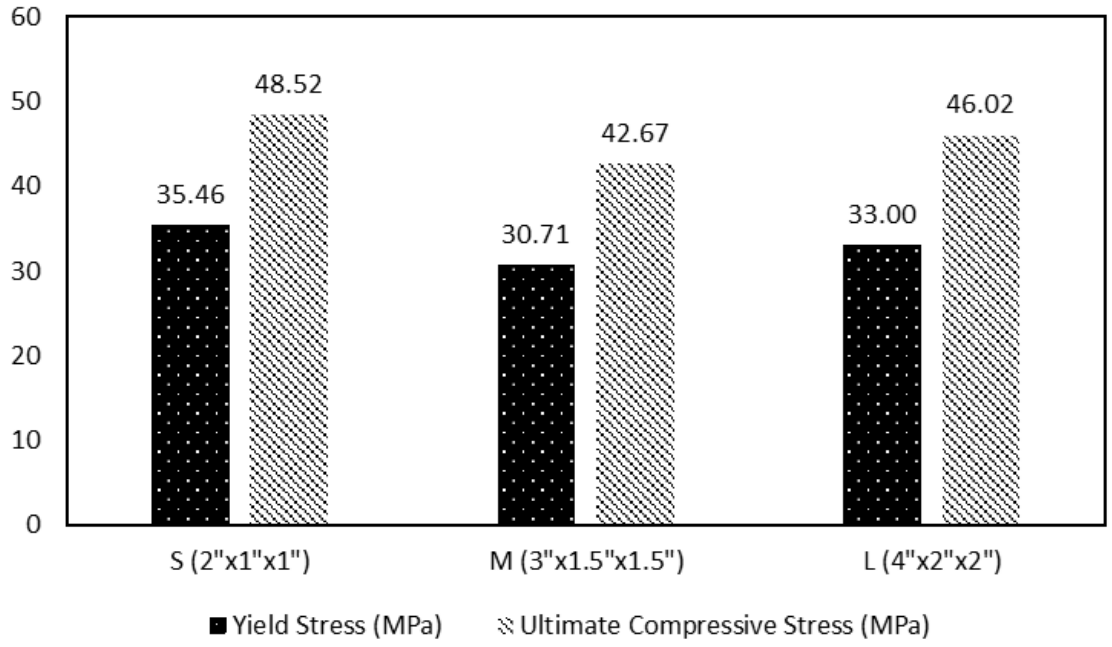

Figure 3-20: Yield stress and ultimate compressive stress values for different size specimens subjected to uniaxial loading.

The size effect is evident in that the larger specimen has the lowest strength and the smallest specimen has the highest strength. However, the medium size has values that do not correspond to what is expected. No interpretation is possible at this time.

All three specimens tested had vertical fractures develop from the tip of the flaw in a similar manner. A series of image frames of the three specimens taken at three time intervals: start of the test (labeled $t_{initial}$), middle of the test (labeled $t_{intermediate}$), and end of the test (labeled t_{final}) along with corresponding sketches are shown in Figure 3-21.

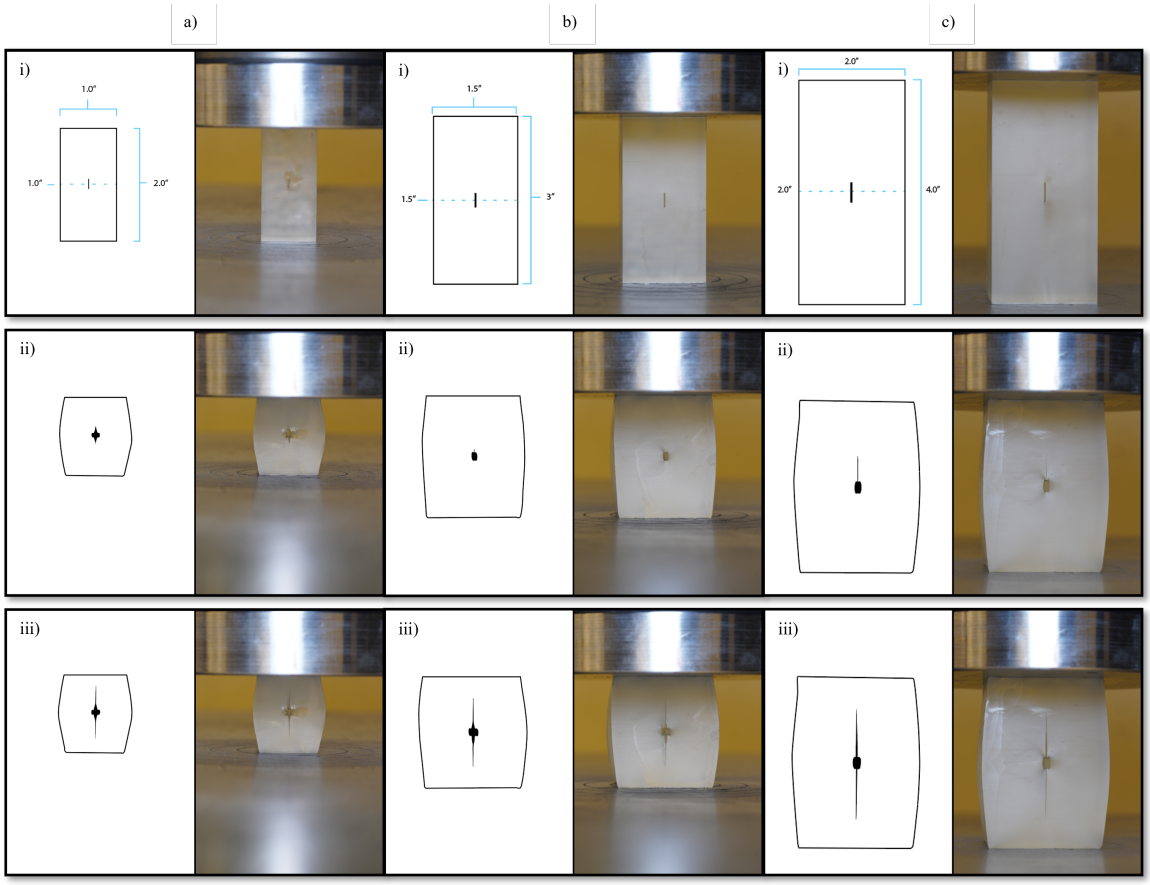

Figure 3-21: Sketch alongside image frame of different size specimens subjected to uniaxial loading at different times: a) S (2"x1"x1"), b) M (3"x1.5"x1.5"), c) L (4"x2"x2"), i) $t_{initial}$, ii) $t_{intermediate}$, and iii) t_{final}.

Medium-sized specimens (3 in x 1.5 in x 1.5 in) were used for the rest of the experiments in this study. This size was selected for two main reasons. First, the small sized specimen required a significantly higher stress for fracture initiation, making it more challenging to induce fracturing. Secondly, the reduced dimensions of the smaller specimen hindered the ability to effectively observe the fracture process and intricate details. Also, the medium sized facilitated reduced material consumption compared to the large specimen, thereby lowering the cost per specimen.

3.4.2 Base Geometry

One of the geometry effects that influence rock testing results is cross-sectional geometry. It is documented in the literature (Hoek and Brown, 2018) that the ultimate compressive stress of rocks increases with the decrease of the slenderness. However, the influence of cross-sectional geometry is not well understood.

To understand this effect, two cross-sectional geometries of prismatic specimens were compared: square and rectangular base. The rectangular base specimen had dimensions (3 in x 1.5 in x 0.75 in) and the square base specimen had dimensions (3 in x 1.5 in x 1.5 in). Figure 3-22 shows the stress-strain data for the two tests at a displacement-controlled loading rate of 1 mm/min.

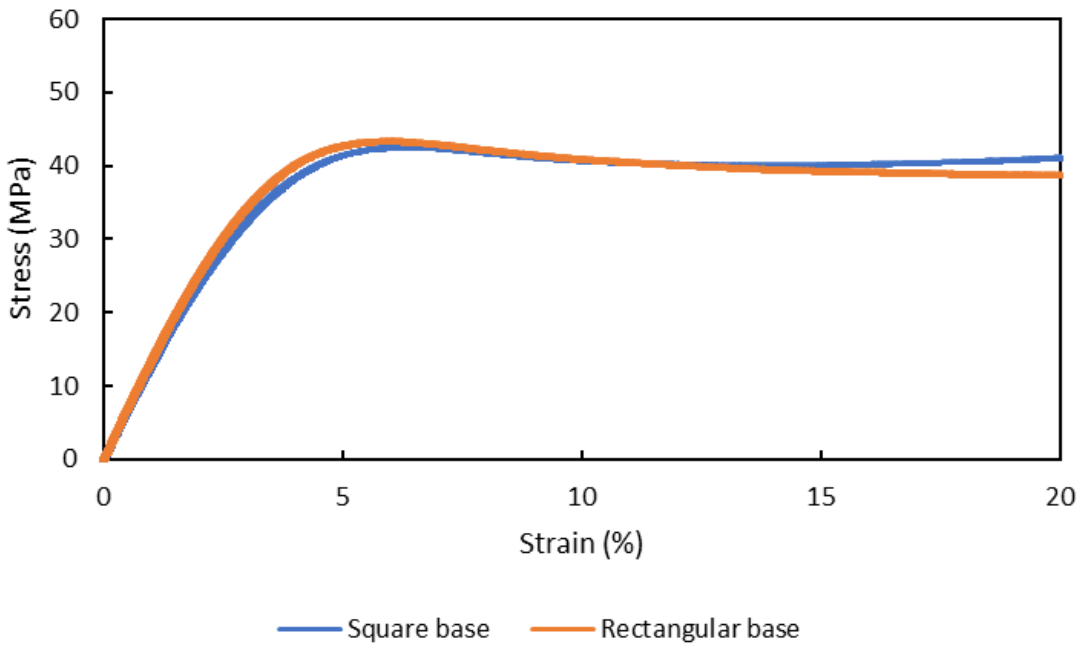

Figure 3-22: Stress-strain data comparing two specimen base geometries subjected to uniaxial loading.

The yield stress and ultimate stress values were determined from the stress-strain plots and are shown below in Figure 3-23.

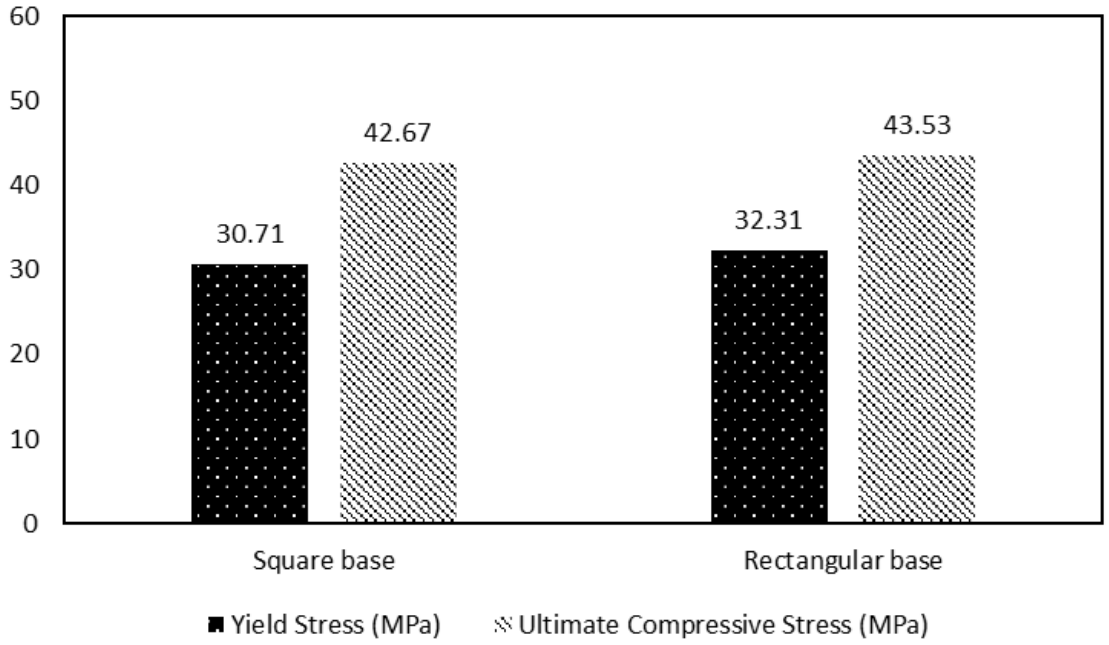

Figure 3-23: Yield stress and ultimate compressive stress values for two specimen base geometries subjected to uniaxial loading.

The results demonstrate that the rectangular base specimen has a slightly higher yield stress and ultimate compressive stress compared to the square base specimen. This may not be only related to the base dimension but also to size difference (e.g., rectangular base specimen has a smaller volume compared to the square base specimen and thus it is expected to have higher strength).

For the square base specimen, buckling was not observed. However, the rectangular base specimen clearly experienced buckling. This was visually apparent at higher loads. Figure 3-24 shows the observed buckling of the rectangular base specimen at high loading.

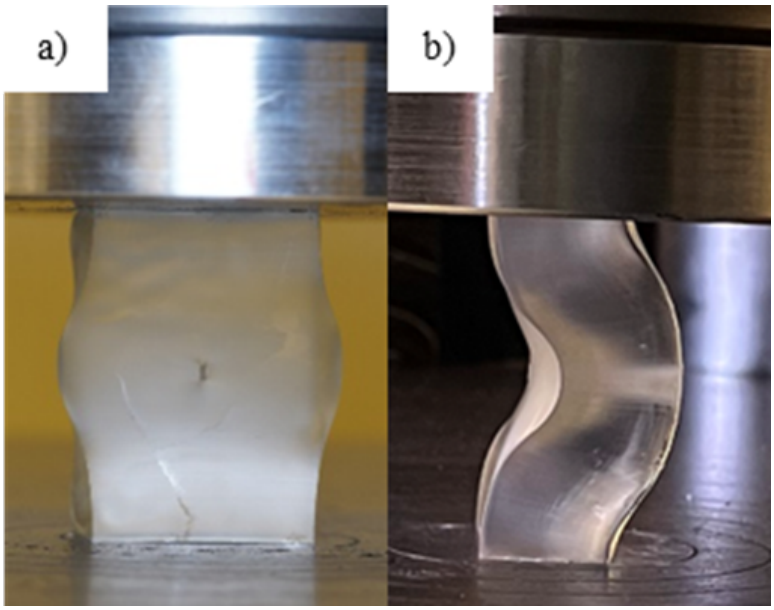

Figure 3-24: Frames of rectangular base specimen subjected to uniaxial loading: a) front view and b) side view.

Square-based specimens were used for the rest of the experiments in this study. This was done to avoid buckling and to minimize the impact of potential end effects or edge-related stress concentrations.

3.5 Boundary Conditions (Frictional End Effects)

The existence of a uniform stress state on loading surfaces, which are usually the principal planes, is a basic assumption in rock testing (Labuz, 1993). During compressive loading, however, this condition does not exactly exist because a frictional constraint develops at the interface between the specimen and loading system. Consequently, the observed response of the specimen may be affected by unknown boundary conditions. Hence, it is important to understand these conditions.

Unconstrained deformation can be achieved by finding an appropriate friction reducer. The friction reducers selected for testing in this study are: silicone-based lubricant, parchment paper, and parafilm. They were applied at both the top and bottom boundaries of the specimen. Figure 3-25 shows the stress–strain curves of the tests with different boundary conditions. The no friction reducer (fixed-end) specimen is also included as a base case for comparison. All four tests were run on identical prismatic specimens with dimensions (3 in x 1.5 in x 1.5 in) at a displacement-controlled loading rate of 1 mm/min.

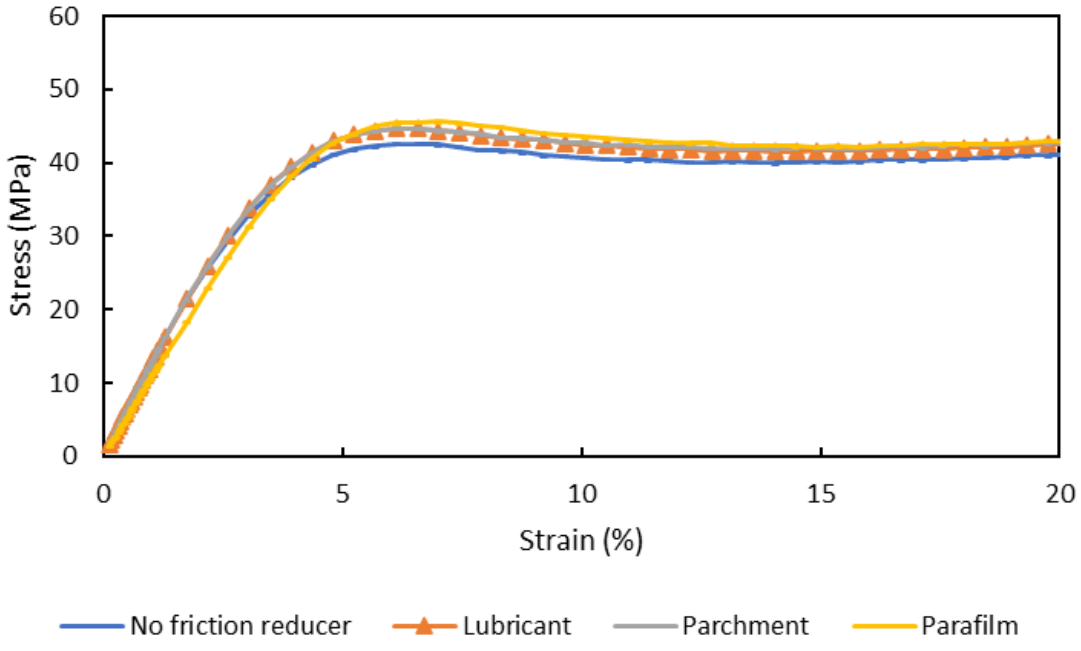

Figure 3-25: Stress-strain data comparing specimens subjected to uniaxial loading with different boundary conditions.

The yield stress and ultimate stress values were determined from the stress-strain plots and are shown below in Figure 3-26.

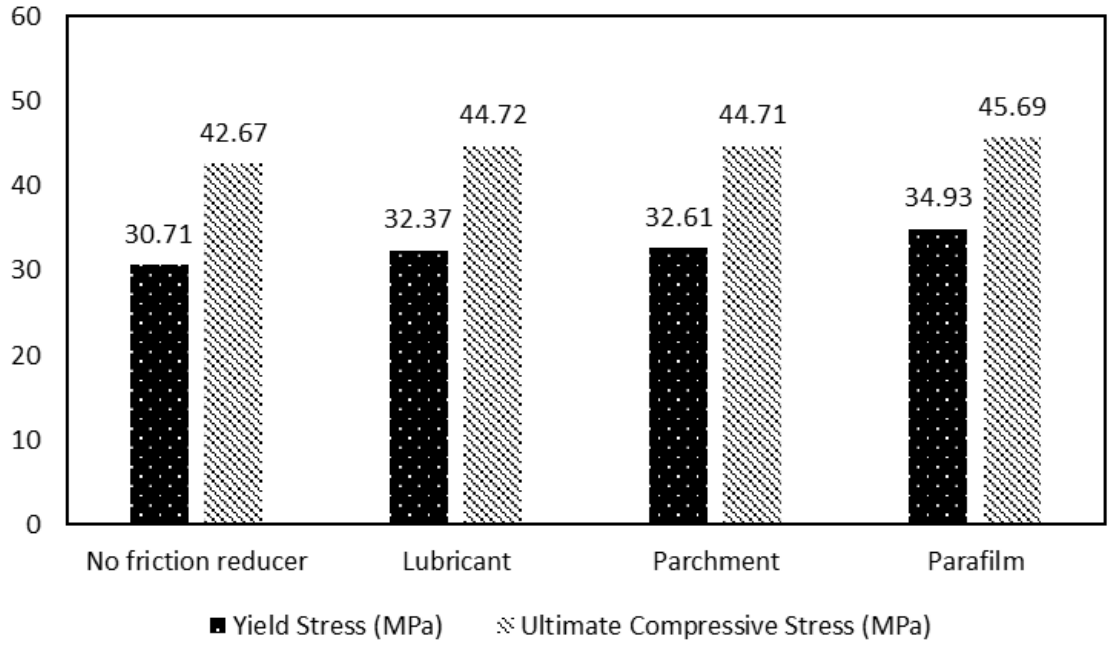

Figure 3-26: Yield stress and ultimate compressive stress values for specimens subjected to uniaxial loading with different boundary conditions.

The results indicate that the specimen with parafilm had the highest yield stress and ultimate compressive stress values, with the parchment and lubricant specimens in between, and the specimen with no friction reducer having the lowest values.

Even with a friction reducer, barreling was evident. This is likely due to frictional constraints development (there may be some friction effects still present). However, these constraints were slightly reduced for the specimens tested with a friction reducer. A sketch of each specimen at 33% strain along with the corresponding image frame is shown in Figure 3-27. Further investigation into other friction reducers could prove useful.

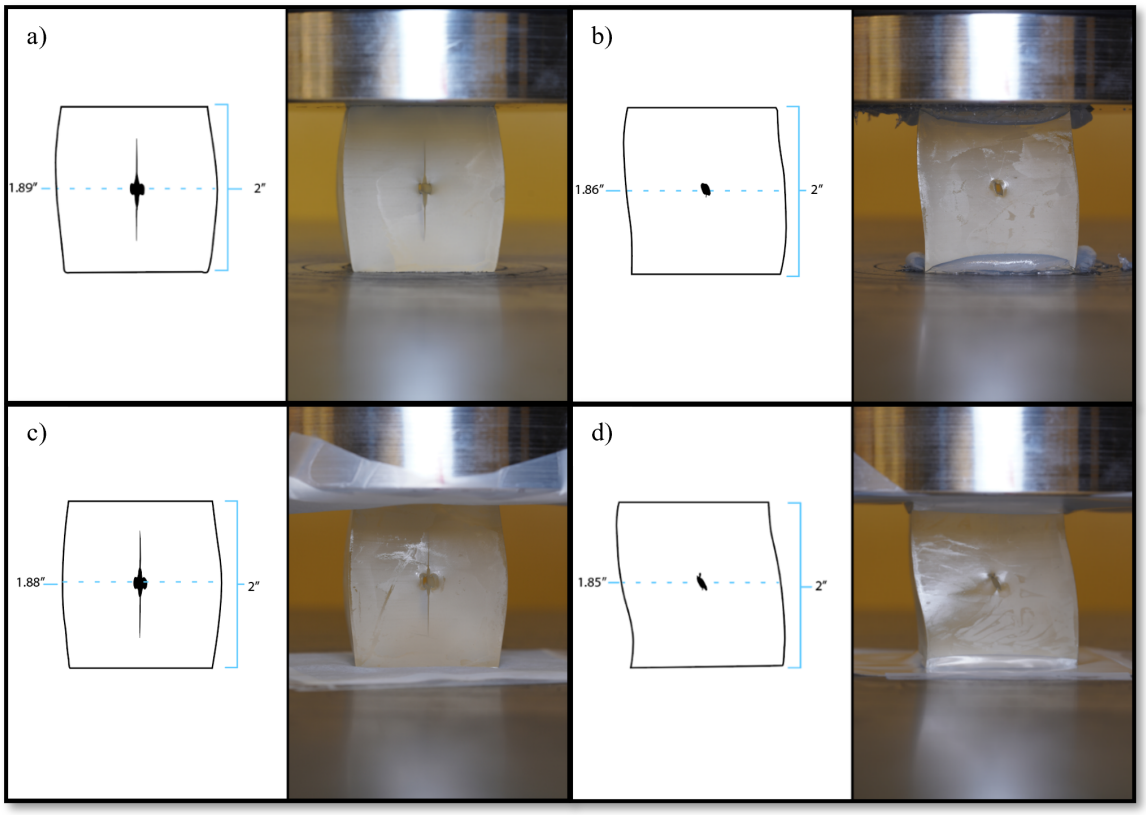

Figure 3-27: Sketch alongside image frame of specimens subjected to uniaxial loading at 33% strain with: a) no friction reducer, b) lubricant, c) parchment, and d) parafilm.

No friction reducer (fixed-end) boundaries were used for the rest of the experiments in this study. This was done as it proved to be the most consistent and practical choice. Suggestions about further investigating other friction reducers are presented in Chapter 4, Section 2 (Future work).

3.6 Flaw Parameters

In most fracture research studies, the pre-existing defect (termed as "flaw") is fully penetrating (e.g., throughgoing). However, in nature, pre-existing flaws in rocks tend to be internal. Although many experimental and theoretical studies have been performed there is still a lack of understanding on the exact mechanisms of many fracture-related processes. An interesting question that has been addressed to some extent is whether the fracture processes in rock experiments with throughgoing flaws are the same as the ones that occur from purely internal flaws. However, a systematic study with completely comparable geometries to our knowledge has not been done.

Fracture testing specimens with internal flaws has been relatively limited compared to specimens with throughgoing flaws for two main reasons. The first is challenges in monitoring the propagation of internal fractures, which requires the use of transparent, artificial materials or advanced imaging techniques, such as X-ray computed tomography due to natural rock's opaque nature. The second is difficulties in producing specimens with controlled internal flaw geometries.

Several techniques have been used by researchers to create specimens with internal flaws and are summarized below:

- Hanging inclusions method. This method, which was used by Dyskin et al. (2003) and Wang et al. (2018), involves two greased aluminum foil disks that are suspended at a specific angle to one of the loading axes within an aluminum mold using copper wires or cotton threads to model a penny-shaped flaw at the center of a resin sample. The resin and catalyst are mixed and poured into the mold, and once cured, samples are cut and polished. Although this method provides good transparency for resin samples, a drawback is the residual presence of holding wires in the samples after casting. The sample preparation using other castable materials is similar by adopting this method.

- Cutting method. First introduced by Adam and Sines (1978) and later used by Dyskin et al. (2003), this method involves creating a penny-shaped flaw by cutting a semi-circular slot into the surface of two sample halves and subsequently gluing them back together. Teflon or greased foil disks are inserted into the slots to ensure contact between the faces. This method is limited in creating multiple initial flaws, as additional cutting planes may introduce instability to the sample and uncertainty in test results, making it suitable only for simple flaw arrangements.

- Laser method. Germanovich et al. (1994) employed a high-energy neodymium-doped laser pulse to introduce internal cracks in non-castable transparent materials like silica glass and PMMA. This method avoids cutting planes and enables the creation of multiple internal flaws but is labor-intensive and requires specialized equipment to achieve the desired flaw arrangement.

- Thermal induction method. Dyskin et al. (2003) utilized thermal induction to create multiple flaws in resin samples by employing an excessively high catalyst ratio, generating considerable heat and thermal stresses. By heating the curing samples in an oven, multiple internal flaws of varying sizes and densities were produced. The method's limitations include the inability to produce elaborately designed flaw arrangements and the presence of residual stresses in resin samples after the curing process.

Specimens can be produced with different flaw specifications using 3D printing technology. A series of experiments are presented comparing the fracturing behavior of specimens containing internal flaws with specimens containing throughgoing flaws at several flaw inclinations. Identical pre-existing quasi-elliptical (ovaloid-shaped) flaws were placed at the center of each specimen. A schematic of specimens with the two types of pre-existing flaws is shown in Figure 3-28.

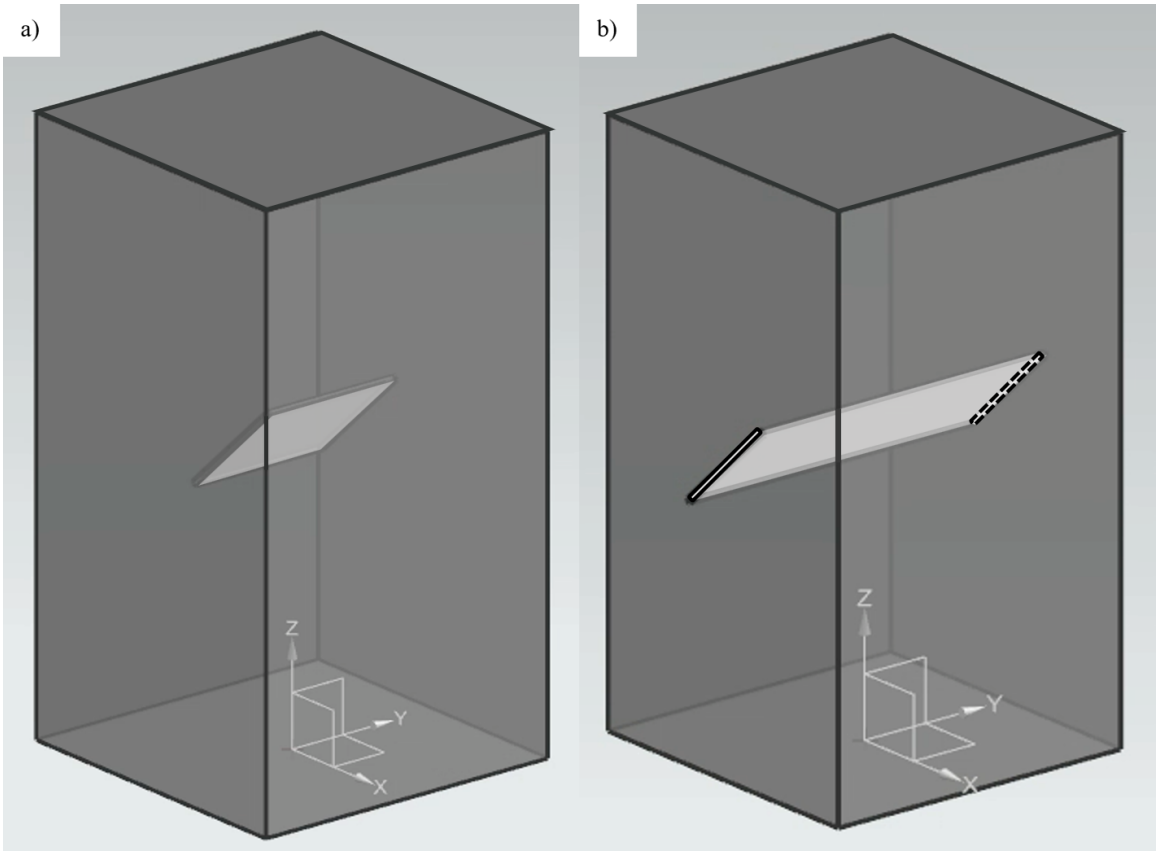

Figure 3-28: Schematic of the two types of pre-existing flaws in the specimens prepared: a) internal flaw and b) throughgoing flaw.

3.6.1 Internal Flaws

The effect of flaw inclination on specimens with internal flaws was investigated by conducting uniaxial tests on five prismatic specimens, each having a different flaw inclination. The flaw inclinations were: 0°, 30°, 45°, 60°, and 90°. Figure 3-29 shows the stress-strain data for the five tests at a displacement-controlled loading rate of 1 mm/min.

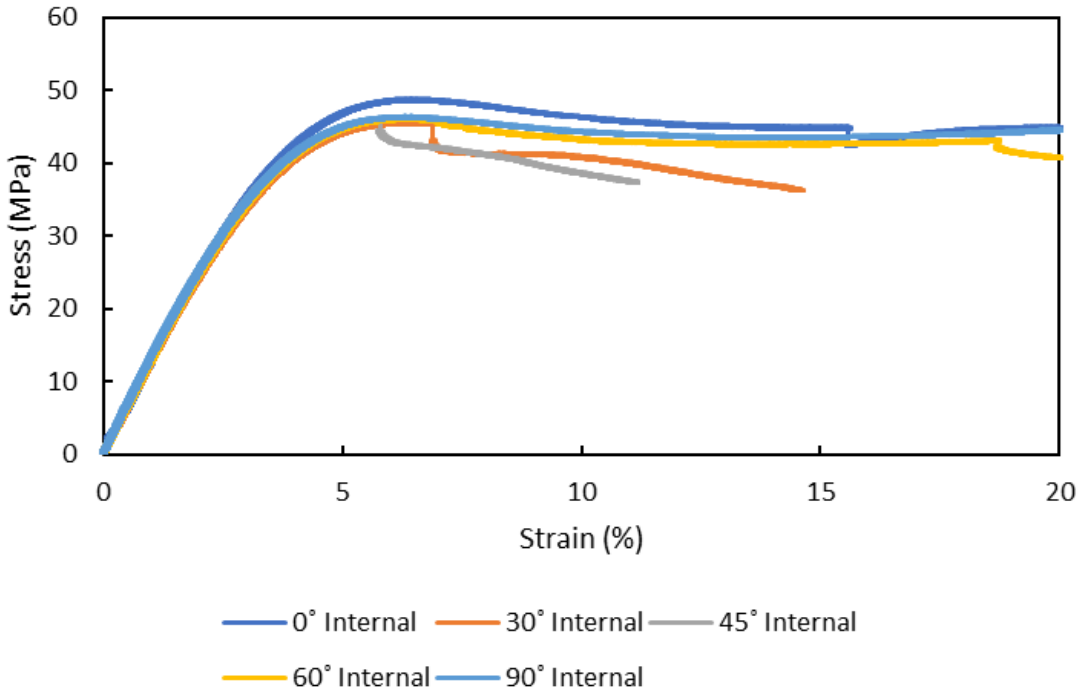

Figure 3-29: Stress-strain data comparing specimens with internal flaws at different flaw inclinations subjected to uniaxial loading.

The yield stress and ultimate compressive stress values were determined from the stress-strain plots and are shown below in Figure 3-30.

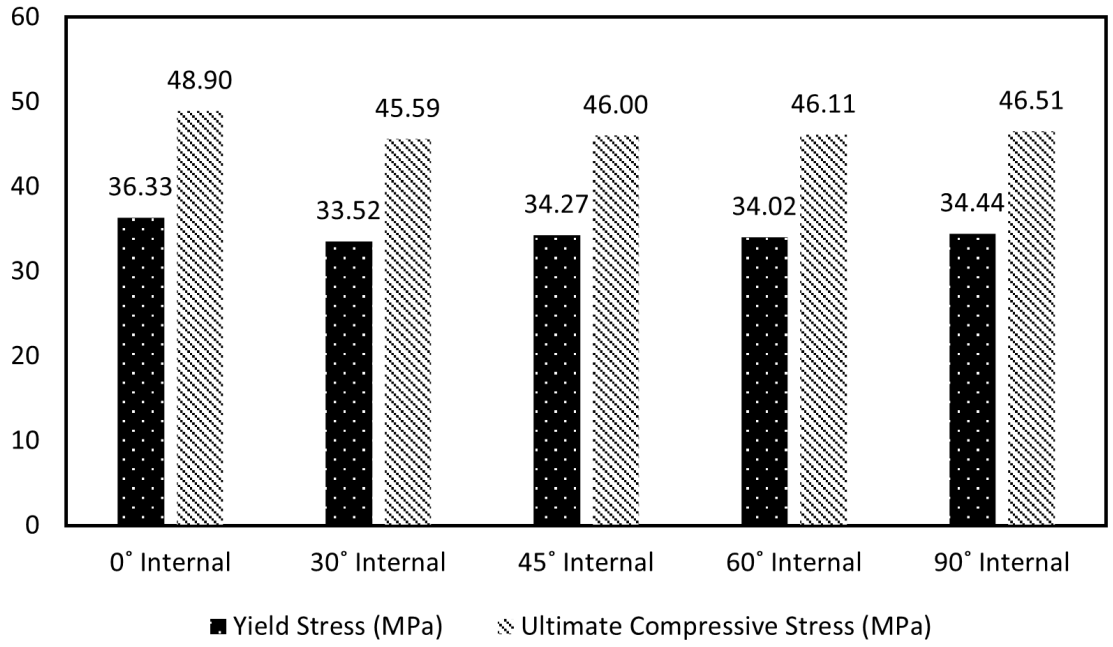

Figure 3-30: Yield stress and ultimate compressive stress values for specimens with internal flaws at different flaw inclinations subjected to uniaxial loading.

Evidently the yield stress and ultimate compressive stress values were influenced by the flaw inclination. This may be attributed to the stress distribution around the flaw changing with the flaw orientation. The results indicate that the specimen with a 0° (horizontal) flaw had the highest yield stress and ultimate compressive stress values, followed by the specimen with a 90° (vertical) flaw in between, and the specimens with intermediate flaw inclinations (30°, 45°, and 60°) having the lowest values. Suggestions about further investigating the stress distributions around the flaws through finite element analysis (FEA) are presented in Chapter 4, Section 2 (Future work).

The cracks produced for each flaw inclination were different. For the 0° (horizontal) flaw specimen, a crack developed in the direction of the diagonal axis of the specimen. For the inclined flaws, wing cracks developed but, interestingly, propagated in a curved trajectory around the flaw. For the 90° (vertical) flaw, a crack propagated in the vertical direction along the axis of compression, as was expected. Image frames of the five specimens with internal flaws taken at: start of the test (labeled $t_{initial}$) and end of the test (labeled t_{final}) are shown in Figure 3-31.

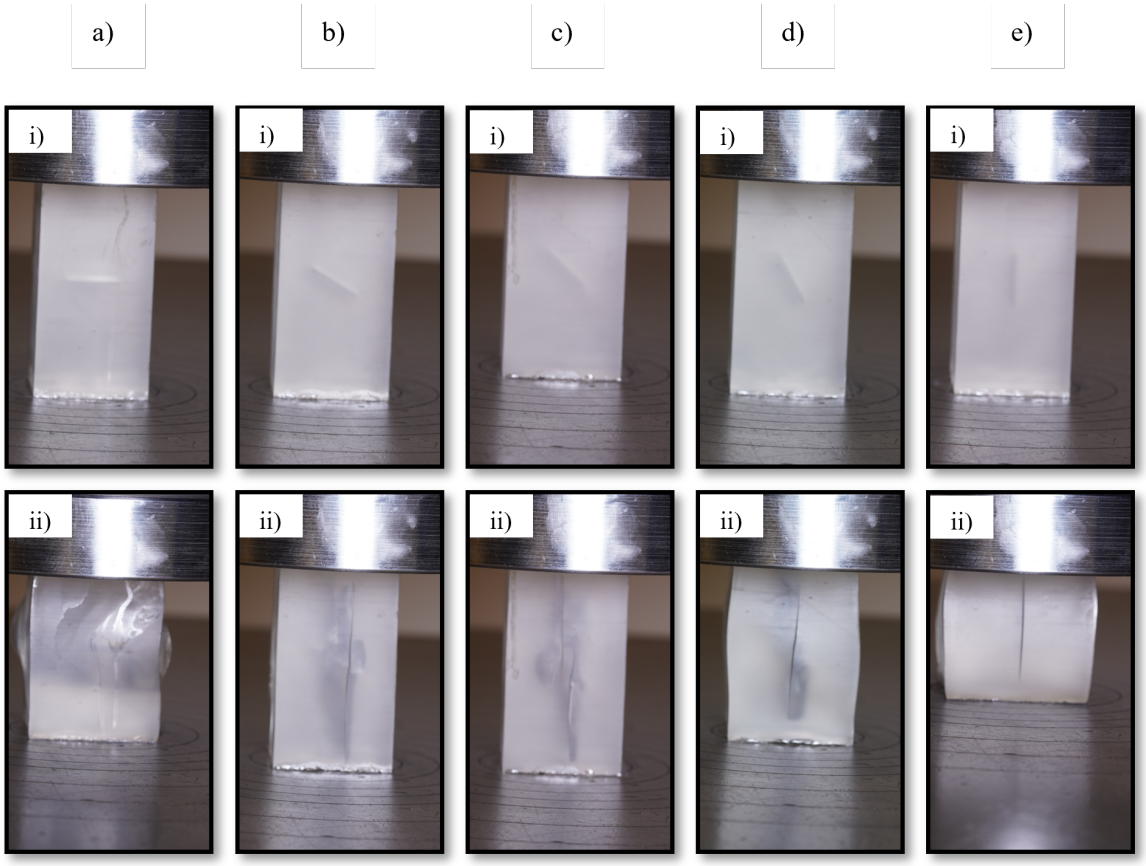

Figure 3-31: Image frames of specimens with internal flaws at different inclinations subjected to uniaxial loading, where: a) 0°, b) 30°, c) 45°, d) 60°, e) 90°, i) $t_{initial}$, and ii) t_{final}.

3.6.2 Throughgoing Flaws

The effect of flaw inclination on specimens with throughgoing flaws was investigated by conducting uniaxial tests on five prismatic specimens, each having a different flaw inclination. The flaw inclinations were: 0°, 30°, 45°, 60°, and 90°. Figure 3-32 shows the stress-strain data for the five tests at a displacement-controlled loading rate of 1 mm/min.

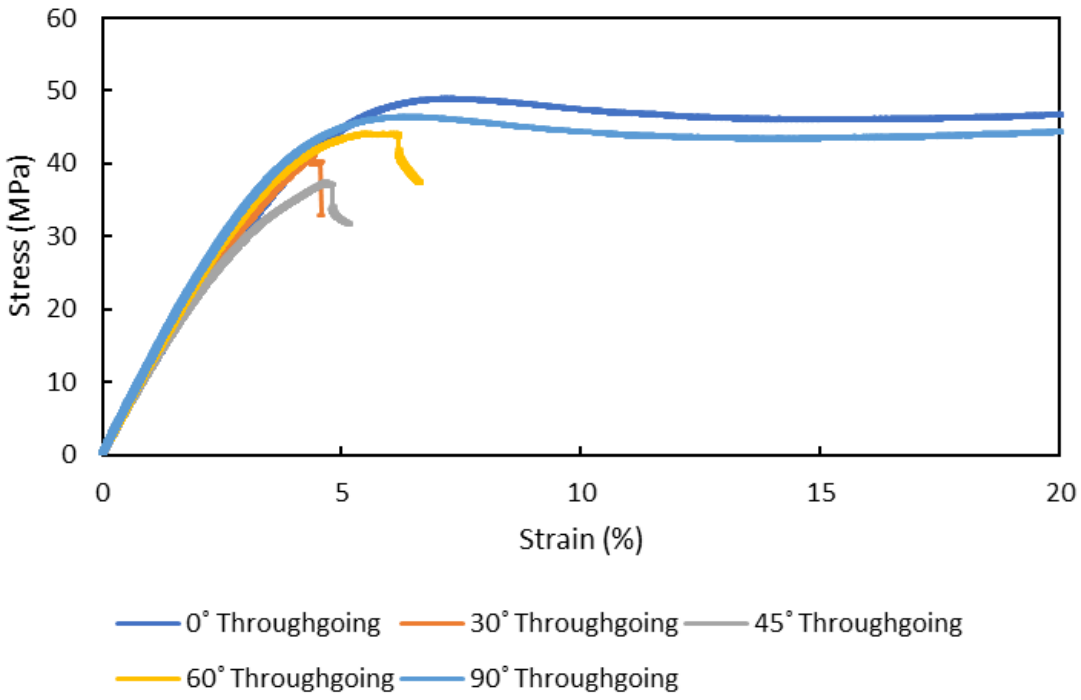

Figure 3-32: Stress-strain data comparing specimens with throughgoing flaws at different flaw inclinations subjected to uniaxial loading.

The yield stress and ultimate compressive stress values were determined from the stress-strain plots and are shown below in Figure 3-33.

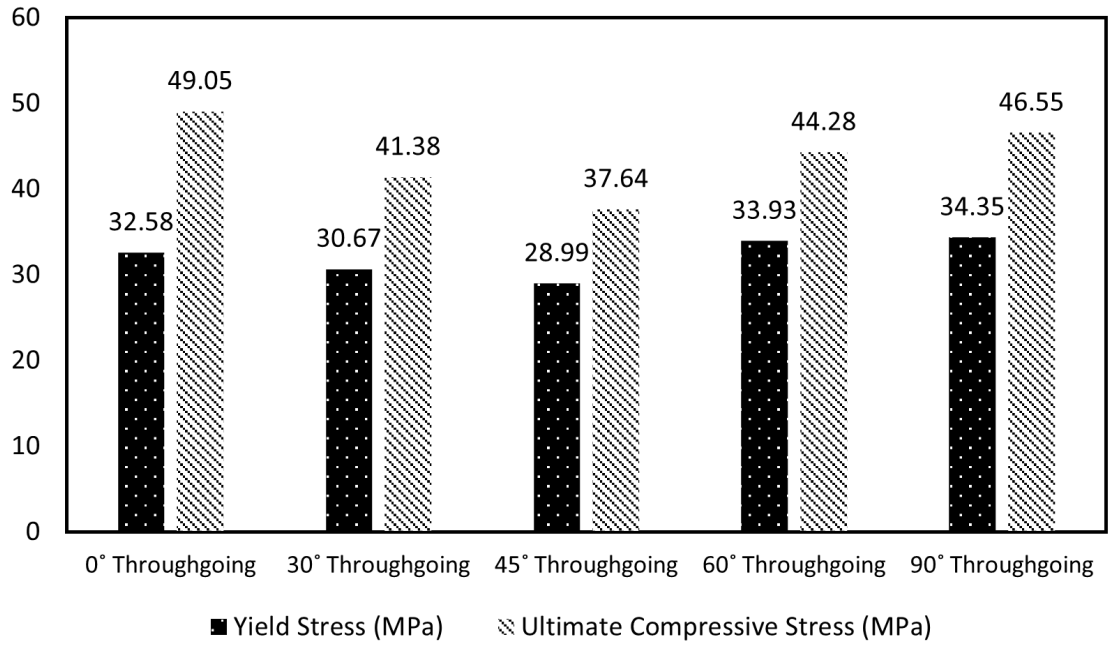

Figure 3-33: Yield stress and ultimate compressive stress values for specimens with throughgoing flaws at different flaw inclinations subjected to uniaxial loading.

The results followed a similar trend as was observed for the internal flaw specimens. The specimen with a 0° (horizontal) flaw had the highest yield stress and ultimate compressive stress values, followed by the specimen with a 90° (vertical) flaw in between, and the specimens with intermediate flaw inclinations (30°, 45°, and 60°) having the lowest values. However, in this case, the 45° inclination had considerably lower yield stress and ultimate compressive stress values among them.

The cracks produced from the specimens with throughgoing flaws at different flaw inclinations showed distinct patterns. For the 0° (horizontal) flaw, a vertical crack developed near the center of the flaw. For the 30° inclined flaw, wing cracks and several branching cracks developed. For the 45° inclined flaw, a more prominent or well-defined wing crack was observed propagating from the tip of the flaw along the axis of compression. For the 60° inclined flaw, cracks similar to those from the 30° inclined flaw were observed but they were at a steeper angle. For the 90° (vertical) flaw, cracks initiated at the flaw edges and propagated vertically. Image frames of the five specimens with throughgoing flaws taken at: start of the test (labeled $t_{initial}$) and end of the test (labeled t_{final}) are shown in Figure 3-34.

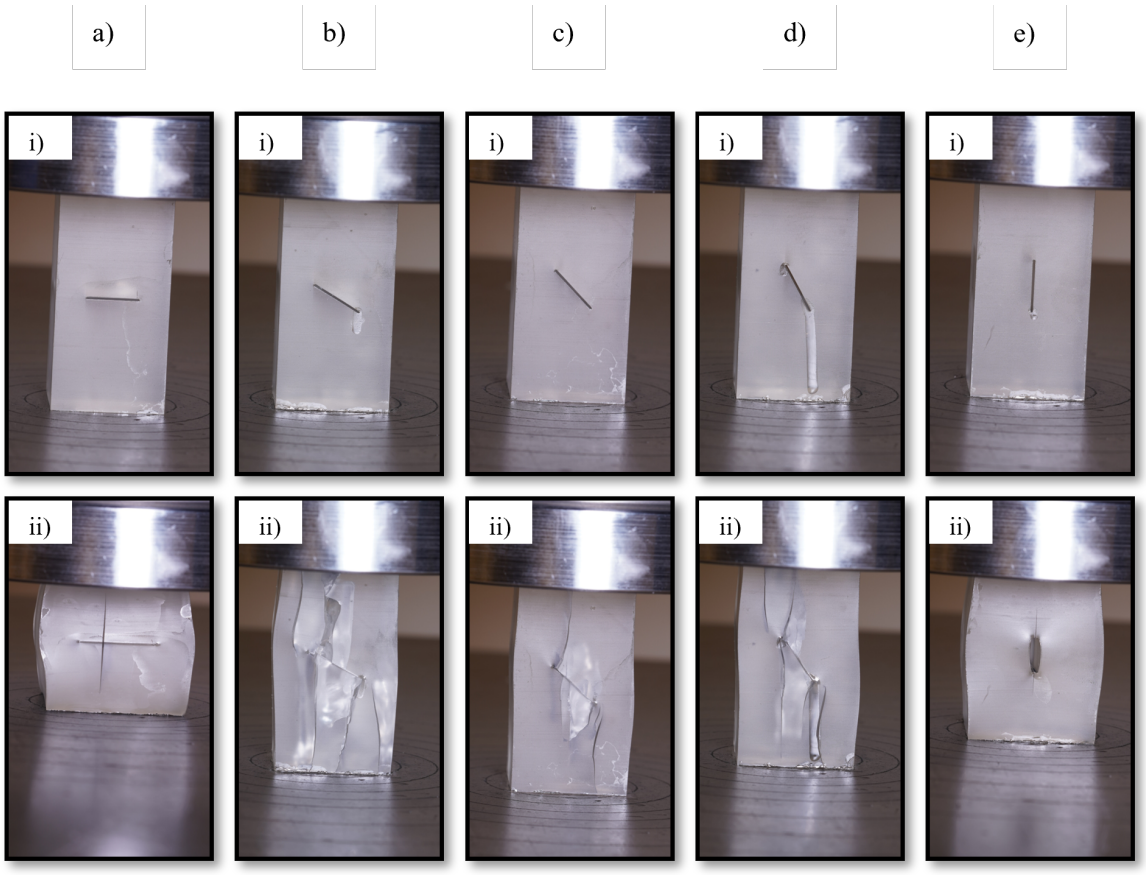

Figure 3-34: Image frames of specimens with throughgoing flaws at different inclinations subjected to uniaxial loading, where: a) 0°, b) 30°, c) 45°, d) 60°, e) 90°, i) $t_{initial}$, and ii) t_{final}.

3.6.3 Comparison of Internal Flaws and Throughgoing Flaws

The yield stress and ultimate compressive stress values for specimens with internal flaws and specimens with throughgoing flaws at the different flaw inclinations are shown below in Figure 3-35.

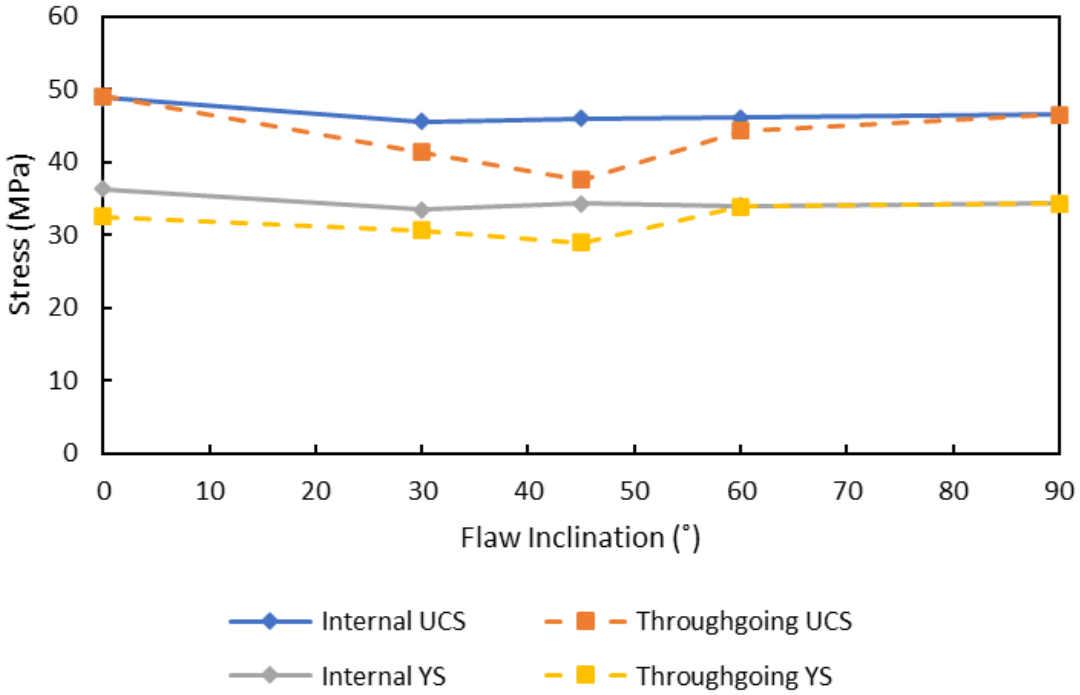

Figure 3-35: Yield stress (YS) and ultimate compressive stress (UCS) values of specimens with internal flaws (solid curves) and specimens with throughgoing flaws (dotted curves) at different flaw inclinations.

The results show that specimens with internal flaws generally exhibit higher yield stress and ultimate compressive stress values than those with throughgoing flaws. A possible explanation for this is that for the specimens with throughgoing flaws, the remaining intact area is smaller than that for the internal flaw specimens. Hence, the stress concentration on the intact area for the throughgoing flaw specimens is higher than the stress concentration for the internal flaw specimens, leading to lower yield strength and ultimate compressive strength values.

Crack initiation and propagation behavior was observed to be different between specimens with internal flaws and specimens with throughgoing flaws. Especially when looking at the inclined (30°, 45°, and 60°) flaw specimens, tensile wing cracks appeared in specimens with throughgoing flaws, while wing cracks with petal cracks were associated with the internal flaws. For throughgoing flaws, the cracks formed from the tips of the flaw and grew in the direction of loading (towards the end of the specimen). On the other hand, for internal flaws, the cracks formed at the tips of the flaw and wrapped around the flaw and formed petal cracks. A similar wrapping effect was observed by Dyskin (1994) and may be a result of principal stresses near the pre-existing flaw acting in a radial direction (Germanovich et al., 1994). A front face view image of the specimens with 45° internal and throughgoing flaws, taken after the experiment and illustrating the difference observed in crack behavior, is shown in Figure 3-36.

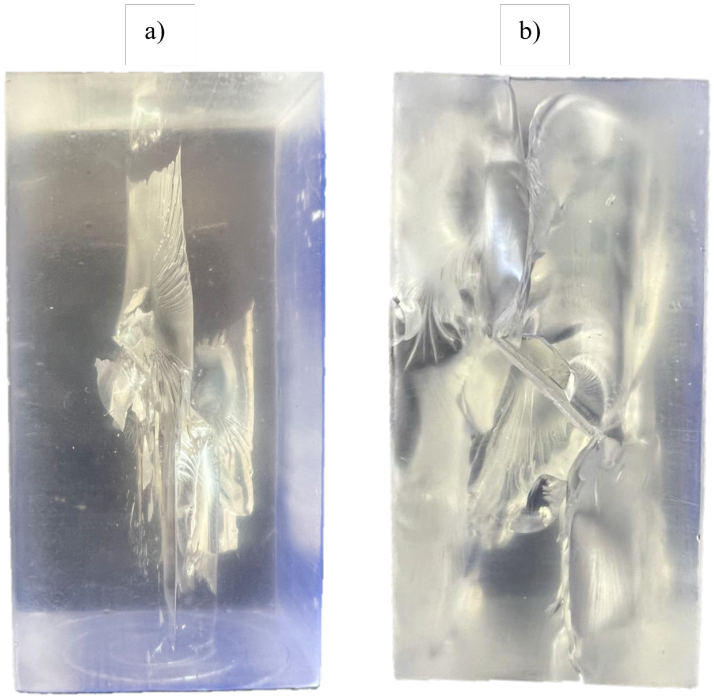

Figure 3-36: Images taken of specimens with 45° a) internal and b) throughgoing flaws after the experiment showing the difference in crack behavior.

A 3D model was developed for the same specimens, with 45° internal and throughgoing flaws, after the experiment and is shown in Figure 3-37.

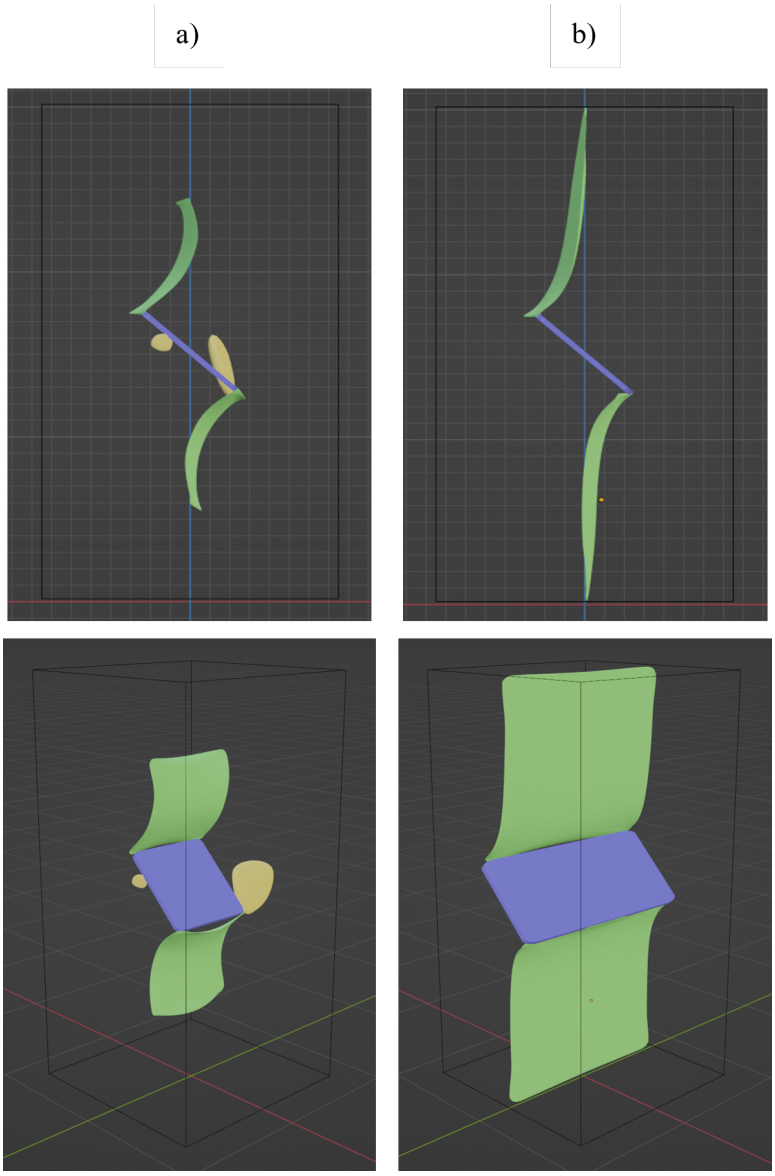

Figure 3-37: Screenshots of 3D model of specimens with 45° a) internal and b) throughgoing flaws after the experiment, showing the difference in crack behavior from the front face and isometric views, respectively. The blue color represents the initial flaw, the green color represents the primary wing cracks, and the yellow color represents the petal cracks.

Chapter 4

Conclusions and Recommendations

4.1 Summary and Conclusions

This research aimed to achieve two main objectives. Firstly, it detailed the apparatus, instrumentation, specimen properties, and procedures used in systematically conducting rock fracturing experiments, focusing on process parameters (post-processing curing and printing orientation), compression platen type (fixed vs. flexible), specimen centering, loading control method (displacement vs. load) and rate, specimen size, cross-sectional geometry, and frictional end effects (fixed vs. lubricated boundaries). Secondly, it carried out a comprehensive study comparing the fracture processes in rock experiments with internal flaws and throughgoing flaws at different flaw inclinations. All the tests were conducted on 3D printed artificial rock specimens.

The results lead to the following conclusions:

- Post-processing curing increased the strength of the material, with longer curing times resulting in higher material strength.
- Different printing orientations exhibited varying strength.
- Comparison of the compression platen types showed mostly an increase in ultimate compressive stress and yield stress values when flexible platens were used. Moreover, using a fixed compression platen helps reduce the bulging of the specimen.

- Centering the specimen is crucial for uniform deformation and reduced bulging.
- The different loading control methods resulted in different strength properties. Specifically, an increase in rate increased the yield stress and ultimate compressive stress values for both load-controlled and displacement-controlled loadings.
- The size effect was evident in that the largest specimen had the lowest strength and the smallest specimen had the highest strength.
- Rectangular base specimens have slightly higher yield stress and ultimate compressive stress compared to square base specimens, but may exhibit buckling at high loads.
- Adding friction reducers at the boundary generally increases strength, though barreling may still occur.
- Differences in crack initiation and propagation exist between internal flaw and throughgoing flaw specimens. This investigation showed that tensile wing cracks appeared in specimens with throughgoing flaws, while wing cracks with petal cracks were associated with the internal flaws. It also showed that the mechanical properties are influenced by the inclination of the flaws and established that specimens with internal flaws generally exhibit higher material strength compared to specimens with throughgoing flaws.

Looking at these different experimental conditions has helped us form a better understanding of how they affect rock fracturing experiments. Testing design and conditions can greatly influence the results. We now know that they matter, so we need to choose them carefully when we test in the future. If we attend to these parameters, we will get the most consistent results.

4.2 Future Work

This work identified several topics of interest that could be further studied:

- There remains a knowledge gap concerning the curing depth of SLA 3D printed resin materials. Existing studies have primarily focused on the general effects of post-processing curing, but a deeper understanding of the specific role of curing depth is needed. Systematic experiments can be conducted by varying curing conditions such as exposure time, UV light intensity, and temperature, and analyzing their effects on curing depth and mechanical properties. Non-destructive testing methods like X-ray computed tomography (CT) or ultrasonic testing can be employed to assess the internal structure of printed specimens and accurately determine curing depth. Electron microscopy, in conjunction with spectroscopy methods like Fourier-transform infrared (FTIR) spectroscopy, can be used to investigate the curing depth and its relationship with the chemical composition and microstructure of printed specimens. Another approach involves slicing the specimens and performing nanoindentation or hardness measurements to examine the material's properties as a function of curing depth. Fracture toughness tests on specimens as a function of depth can also provide valuable insights into the impact of curing depth on fracture resistance and crack propagation behavior. Additionally, the aging effect, which refers to the changes in material properties over time, can be investigated using the same methodology.

- Although the friction reducers tested in this work have led to a reduction in frictional constraints, complete elimination of these constraints has not been achieved. Further research into different friction reducers can potentially yield a more effective solution, minimizing barreling and allowing for more accurate characterization of the material's mechanical properties. A systematic evaluation of various friction reducers, including different materials, coatings, and lubricants, can help identify the most suitable option for specific testing conditions. Incorporating circumferential or "hoop" strain measurements at the top and mid-height of the specimens can aid in understanding the effects of

friction reducers on the deformation behavior and stress distribution within the specimens.

- Comparing the stress fields of specimens with internal and throughgoing flaws can provide insights into how the flaws affect the stress distribution and help understand the differences in their mechanical behavior. Photoelasticity is an experimental technique used to visualize and compare the stress distribution or stress fields within transparent materials, such as polymers or glasses, subjected to mechanical loads. When a specimen is subjected to a load, it undergoes deformation, and the resulting stress distribution within the material can be investigated using photoelasticity. The technique is based on the principle of birefringence, which causes the refractive index of the material to vary with the applied stress. When a polarized light is passed through the specimen, the light's path is altered according to the stress distribution, and the changes in the refractive index result in different colors when observed under a polariscope.

- Finite element analysis (FEA) can also be utilized to evaluate the effect of an internal flaw versus a throughgoing flaw on the stress state around the flaw in the tested specimens. By creating a numerical model that simulates the tested specimens, FEA also allows us to investigate the stress distribution and concentration around the flaws under the applied loading conditions. This computational approach provides valuable insights into the complex stress fields generated by the interaction between the flaw inclination and the applied load. Furthermore, FEA can be used to identify and quantify stress concentrations at the tips of the flaws, which directly affect crack initiation and propagation. Ultimately, such analysis facilitates a better understanding of the relationship between flaw inclination and mechanical properties, such as yield stress and ultimate compressive stress, thereby enhancing the interpretation of experimental results.

Appendix A

Yield Stress Determination Using the 0.2% Method

Yield stress, also known as yield strength, is a material property that represents the stress at which a material begins to deform plastically, or permanently, under applied loads. Up to the yield stress, the material undergoes elastic deformation, meaning that it will return to its original shape once the load is removed. Beyond the yield stress, the material experiences plastic deformation, and any further deformation will result in permanent changes to the material's shape, even after the load is removed.

Yield stress is an important characteristic in materials science and engineering, as it helps to determine the allowable stress that a material can withstand without undergoing permanent deformation. The 0.2% offset method is a widely-used technique to determine the yield stress of a material, particularly for materials that do not exhibit a well-defined yield point, as it provides a consistent and standardized approach to determine the yield stress for comparison. This method is based on estimating the stress at which the material has undergone a small, but permanent, plastic deformation, typically defined as 0.2% of the original length.

To apply the 0.2% offset method, follow these steps:

1. Perform a compressive (or tensile) test on the material to obtain a stress-strain curve.

2. Identify the linear elastic region of the stress-strain curve, where the material obeys Hooke's Law (stress is proportional to strain).

3. Construct a line parallel to the linear elastic region, but offset by 0.2% strain on the strain axis. This represents a small, but permanent, deformation in the material.

4. Determine the point where the offset line intersects the stress-strain curve. The stress value at this intersection is the 0.2% offset yield stress.

An example plot demonstrating this method is shown in Figure A-1.

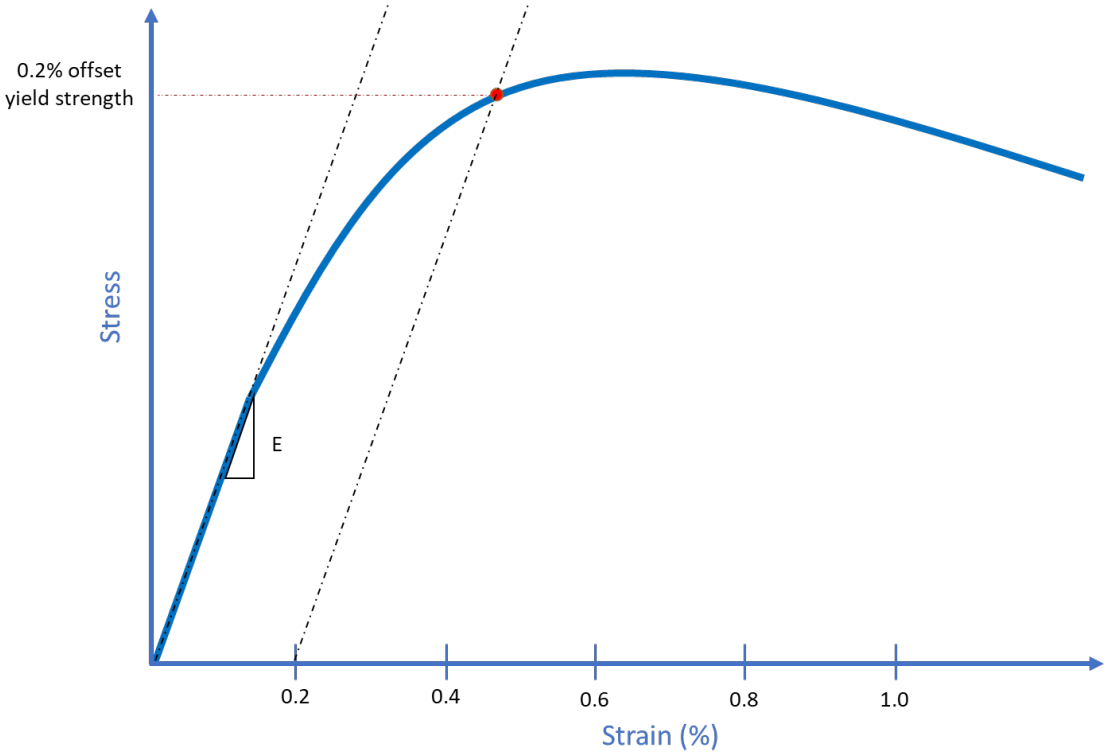

Figure A-1: Example plot illustrating how to determine the yield stress of a material using the 0.2% offset method.

Bibliography

1. Adams, M., and Sines, G. (1978). Crack extension from flaws in a brittle material subjected to compression. Tect., 49(1–2), 97–118.
2. American Society for Testing and Materials. (2017). Standard Test Methods for Compressive Strength and Elastic Moduli of Intact Rock Core Specimens under Varying States of Stress and Temperatures. ASTM International. https://www.astm.org/d7012-14e01.html
3. Baecher, G. B., and Einstein, H. H. (1981). Size effect in rock testing. Geophys. Res. Lett., 8(7): 671–674.
4. Bobet, A. (1997). Fracture coalescence in rock materials: experimental observations and numerical predictions. Doctoral dissertation, Massachusetts Institute of Technology.
5. Dyskin, A. V., Jewell, R. J., Joer, H., Sahouryeh, E., and Ustinov, K. B. (1994). Experiments on 3-D crack growth in uniaxial compression. Int. J. of Fract., 65(4), R77–83.
6. Dyskin, A. V., Sahouryeh, E., Jewell, R. J., Joer, H., and Ustinov, K. B. (2003). Influence of shape and locations of initial 3-D cracks on their growth in uniaxial compression. Eng. Fract. Mech., 70(15), 2115–2136.
7. Gao, Y., Wu, T., and Zhou, Y. (2020). Application and prospective of 3D printing in rock mechanics: A review. Int. J. Miner. Metall. Mater., 28(1): 1–17.
8. Germanovich, L. N., Salganik, R. L., Dyskin, A. V., and Lee, K. K. (1994). Mechanisms of brittle fracture of rock with pre-existing cracks in compression. Pure Appl. Geophys., 143(1–3), 117–149.
9. Glucklich J. and Cohen L.J. (1968). Strain energy and size effects in a brittle material. Mater. Res. Standards, 8: 17–22.
10. Gonçalves da Silva, B. M. (2009). Modeling of crack initiation, propagation, and coalescence in rocks. Master's thesis, Massachusetts Institute of Technology.
11. Hamzah, H. H., Shafiee, S. A., Abdalla, A., and Patel, B. A. (2018). 3D printable conductive materials for the fabrication of electrochemical sensors: A mini review. Electrochem. Commun., 96: 27–31.
12. Hoek, E., and Brown, E. T. (2019). The Hoek–Brown failure criterion and GSI –2018 edition. J. Rock Mech. Geotech. Eng.,11(3): 445–463.
13. Isah, B. W., Mohamad, H., Ahmad, N. R., Harahap, I. S. H., and Al-Bared, M. A. M. (2020). Uniaxial compression test of rocks: Review of strain measuring instruments. IOP Conf. Ser.: Earth Environ. Sci., 476(1).

14. ISRM. (2007). The complete ISRM suggested methods for rock characterization, testing and monitoring: 1974–2006. Ulusay & Hudson, Ankara, 1st Edition.
15. Kodama, H. (1981). Automatic method for fabricating a three-dimensional plastic model with photo-hardening polymer. Rev. Sci. Instrum., 52(11), 1770–1773.
16. Komurlu, E. (2018). Loading rate conditions and specimen size effect on strength and deformability of rock materials under uniaxial compression. Int. J. Geo. Eng., 9(1).
17. Kong, L., Ostadhassan, M., Li, C., and Tamimi, N. (2018). Can 3-D Printed Gypsum Samples Replicate Natural Rocks? An Experimental Study. Rock Mech. Rock Eng., 51(10): 3061–3074.
18. Labuz, J. F., and Bridell, J. M. (1993). Reducing frictional constraint in compression testing through lubrication. Int. J. Rock Mech. Mining Sci. & Geom. Absts., 30(4): 451–455.
19. Marin, E., Boschetto, F., Zanocco, M., Doan, H. N., Sunthar, T. P. M., Kinashi, K., Iba, D., Zhu, W., and Pezzotti, G. (2021). UV-curing and thermal ageing of methacrylated stereo-lithographic resin. Polym. Degrad. Stab., 185: 109503.
20. Melchels, F. P. W., Feijen, J., and Grijpma, D. W. (2010). A review on stereolithography and its applications in biomedical engineering. Biomaterials, 31(24): 6121–6130.
21. Miller, J. T. (2008). Crack coalescence in granite. Master's thesis, Massachusetts Institute of Technology.
22. Morgan, S. P. (2015). An experimental and numerical study on the fracturing processes in Opalinus shale. Doctoral dissertation, Massachusetts Institute of Technology.
23. Ngo, T. D., Kashani, A., Imbalzano, G., Nguyen, K. T. Q., and Hui, D. (2018). Additive manufacturing (3D printing): A review of materials, methods, applications and challenges. Compos. B Eng., 143: 172–196.
24. Reyes, O. M. L. (1991). Experimental study and analytical modelling of compressive fracture in brittle materials. Doctoral dissertation, Massachusetts Institute of Technology.
25. Riccio, C., Civera, M., Grimaldo Ruiz, O., Pedullà, P., Rodriguez Reinoso, M., Tommasi, G., Vollaro, M., Burgio, V., and Surace, C. (2022). Effects of Curing on Photosensitive Resins in SLA Additive Manufacturing. Appl. Mech. 2021, 2, 942–955. Appl. Mech., 3(1): 123–124.
26. Vaezi, M., Seitz, H., and Yang, S. (2012). A review on 3D micro-additive manufacturing technologies. Int. J. Adv. Manuf., 67(5–8): 1721–1754.
27. Wang, H., Dyskin, A., Pasternak, E., Dight, P., and Sarmadivaleh, M. (2018). Effect of the intermediate principal stress on 3-D Crack Growth. Eng. Fract. Mech., 204, 404–420.
28. Wang, L., Ju, Y., Xie, H., Ma, G., Mao, L., and He, K. (2017). The mechanical and photoelastic properties of 3D printable stress-visualized materials. Sci. Rep., 7(1).
29. Watters, M. P., and Bernhardt, M. L. (2018). Curing parameters to improve the mechanical properties of stereolithographic printed specimens. Rapid Prototyp. J., 24(1): 46–51.

30. Weibull, W. (1939). A Statistical Theory of the Strength of Materials. Stockholm, 1st edition.
31. Wong, L. N. Y. (2008). Crack coalescence in molded gypsum and Carrara marble. Doctoral dissertation, Massachusetts Institute of Technology.
32. Xu, H., Zhou, W., Xie, R., Da, L., Xiao, C., Shan, Y., and Zhang, H. (2016). Characterization of Rock Mechanical Properties Using Lab Tests and Numerical Interpretation Model of Well Logs. Math. Probl. Eng., 2016: 1–13.
33. Zhou, T., and Zhu, J. B. (2018). Identification of a Suitable 3D Printing Material for Mimicking Brittle and Hard Rocks and Its Brittleness Enhancements. Rock Mech. Rock Eng., 51(3): 765–777.